UNIVERSITÀ DEGLI STUDI DI PADOVA

Dipartimento di Fisica e Astronomia "Galileo Galilei"

Dipartimento di Geoscienze

Corso di Laurea Magistrale in Astronomia

Master Thesis

Analysis of Martian north polar ice cap layering with SHARAD data

Relatore
Prof. Matteo Massironi
Correlatore
Dr. Luca Penasa

Laureanda
Giulia Lovati

Anno Accademico 2019/2020

A duč chei che se senti,
almancu snal,
sot Narlä.

ABSTRACT

Martian polar ice caps are characterized by layered deposits, mainly composed of water ice and a small percentage of dust sediments. Past investigations found that the layering periodicities can be connected with variations of Mars orbital parameters, because of the orbital forcing phenomenon (Becerra, Sori, and Byrne 2017).

The periodicities quantification has already been made with the study of three different types of stratigraphic observations: layer protrusion, local slope and layer brightness versus depth (Becerra, Sori, and Byrne 2017). This investigation is possible only where the layering emerges at the surface and where high resolution DTMs are available. In order to extend this type of study inside the whole cap, in this work we use SHARAD (Mars Reconnaissance Orbiter, NASA) radar data. The stratification inside the cap is indeed well visible in the radargrams, thanks to the contrast of dielectric constants of the different layers.

We decided to isolate the subsurface regions of the North Polar Layered Deposits (NPLD) where the stratification is more evident and the signal is more intense, namely the ones that are nearest to the polar surface. Once isolated, we studied their layering periodicities.

With this purpose, we developed a semi-automated method to elaborate the radar sections. We use the Labeling of Connected Component technique, applied to radar images, segmented through thresholding. Once isolated, we obtained the strata periodicities inside these regions, through Time Series Analysis, and we compared them to the orbital parameters periodicities provided by Laskar, Correia, et al. 2004 simulations.

From the analysis of our data, we found three main strata periodicities of approximately 70, 41 and 29 m, that are partly consistent with the two values found from the superficial outcrops (Becerra, Sori, and Byrne 2017). Most importantly, our 1° and 3° periodicities appear to be in agreement with the obliquity and precession variations, suggesting that a possible link with the orbital forcing phenomenon can be detected.

CONTENTS

1 INTRODUCTION

The *Polar Layered Deposits* are specific regions of the *Martian Polar Caps*. They are characterized by hundreds of layers, mainly composed of water ice and a small percentage of dust sediments (less then 5% , Grima et al. 2009).

The polar layered deposits represent an optimal target for missions equipped with *radar* instruments. This type of technology allows to visualize the stratification underneath the polar surface. In fact, each layer has a specific *permittivity* value, depending on its composition. This means that the radar signal, penetrating the cap, can be reflected on alternating surfaces where strong discontinuities are present.

These regions are particularly important because they contain the information about the *past climate conditions* on the planet. Each layer's characteristics depend on climatic conditions of its formation period.

There is the hypothesis that one phenomenon that affects the formation of this layering is the *orbital forcing* phenomenon, i.e. the physic process in which the variation of Mars orbital parameters influence the *insolation curve*, and therefore the planet's *climate conditions*. The two parameters that seem to have the major influence on martian climate are the *obliquity* and the *argument of perihelion*, having oscillation periods respectively of ~ 120 kyr and ~ 51 kyr (Becerra, Sori, and Byrne 2017).

In this work will be presented the study of the *North Polar Layered Deposits (NPLD)*, thanks to *SHARAD radar data* (Mars Reconnaissance Orbiter, NASA). The aim is to is to find out if there is a correlation between the variation of Mars orbital parameters and the occurrence of these strata, and therefore what is the entity of the orbital forcing phenomenon on Mars.

The choice to focus on the *North* Polar Cap has been made because it results younger (4-5 Myr Christine Schøtt Hvidberg et al. 2012) with respect to the Southern one (dated between 7-14 Myr Ken E Herkenhoff and Plaut 2000, and 30-100 Myr Koutnik et al. 2002). This makes the connection with the orbital parameter evolution simpler, because Laskar, Correia, et al. 2004 simulations show that the obliquity evolution is strongly chaotic. Thus it is possible to make precise simulations only for the last 20 Myr.

In order to make this analysis, we isolate the subsurface regions of the NPLD where the stratification is more evident and the signal is more intense, namely the ones that are nearest to the polar surface. Once isolated, we studied their layering periodicities.

With this purpose, we developed a *semi-automated method* to elaborate the radar sections. We use the *Labeling of Connected Component* technique, applied to radar images, segmented through *thresholding*. In this way we can select and isolate the wider components that, in fact, correspond to the most evident stratified regions, because they result more brighter and extended then the rest of the image.

Once isolated, we obtained the strata periodicities inside these regions, through *Time Series Analysis*, and we compared them to the orbital parameters periodicities provided by Laskar, Correia, et al. 2004 simulations.

Another part of the work is the visualization of the *three-dimensional structure* of the layers, in order to highlight the coherency between neighboring radar sections. Having an idea of the extension of the strata is very important if we want to draw conclusions on the mechanisms that led to their formation: if they were local mechanisms or more global ones, able to affect the entire cap.

Decoding the information contained into these strata will help us to deepen the climatic evolution and the entity of the orbital forcing phenomenon on Mars. This could be useful both from the *geophysical* and the *exoplanetary* point of view, because

it helps us to understand better the influence of this phenomenon on the climate history of another terrestrial planet, with an atmospheric system that is relatively simpler with respect to the one that we find on Earth, largely influenced by biosphere and hydrosphere.

2 MARTIAN POLAR ICE CAPS

2.1 OVERVIEW

We can distinguish different regions that compose the maritan polar caps, each one characterized by its own particular timescale:

- the *Polar Layered Deposits (PLD)*, kilometer-thick stratified sheet, mainly composed of water ice and mineral sediments (highlighted in Figure 3).
- the *Northern Residual Cap*, a layer of nearly pure water ice that interacts with the atmosphere and covers the northern PLD.
- the *Southern Residual Cap*, composed of CO_2 ice, several meters thick, sitting upon a substrate of water ice.
- a seasonal *dry ice* superficial layer, a few tens of centimeters thick, produced by the seasonal transfer of CO_2 between the atmosphere and the surface. The southern cap maintains part of the CO_2 ice layer continually, because of its higher altitude and lower temperature.

Initially the composition of the caps was not very clear. In 1966, when the first Mars spacecraft, *Mariner 4* (NASA), determined that the martian atmosphere was largely composed by carbon dioxide, it was thought that both polar caps should have consisted largely of frozen carbon dioxide too, with only a small amount of water ice. It was only with the *Viking* orbiters (both launched in 1975) and, subsequently, with high-resolution and thermal images from *Mars Global Surveyor* (launched in 1996) and *Mars Odyssey* (launched in 2001), respectively, that the knowledge that the Martian polar caps consist almost entirely of water ice was gradually confirmed.

Seasonal dry ice is a powerful mean to study, every year, the annual variations in the *Martian atmosphere*. Among the many effects it causes, the seasonal transfer of CO_2 between the polar caps and the atmosphere, freezing out onto the caps in winter and subliming in spring and summer, makes the *surface pressure* change of around 25%, over an annual cycle (Thomas et al., 2019). Furthermore, it produces many small-scale phenomena, like gas jets activity, accompanied bu dust transport (Kieffer et al., 2006), or gully-formations (Pilorget and Forget, 2016).

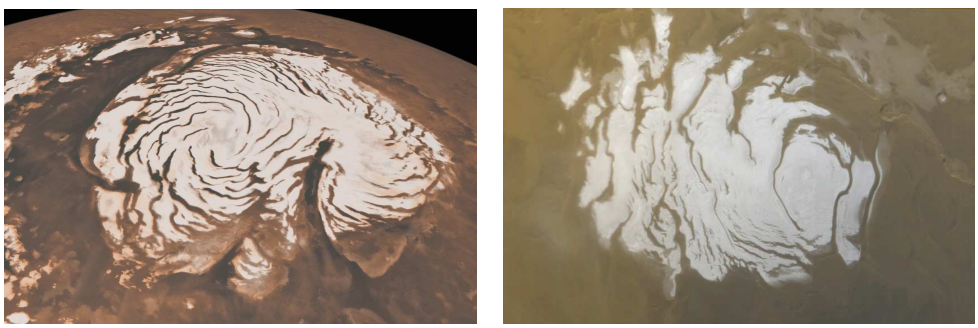

(a) *North polar cap. Image Credit: Mars Global Surveyor, NASA*

(b) *South polar cap. Image Credit: Mars Global Surveyor, NASA*

Figure 1: Martian polar caps. In both caps we can see the Spiraling Troughs.

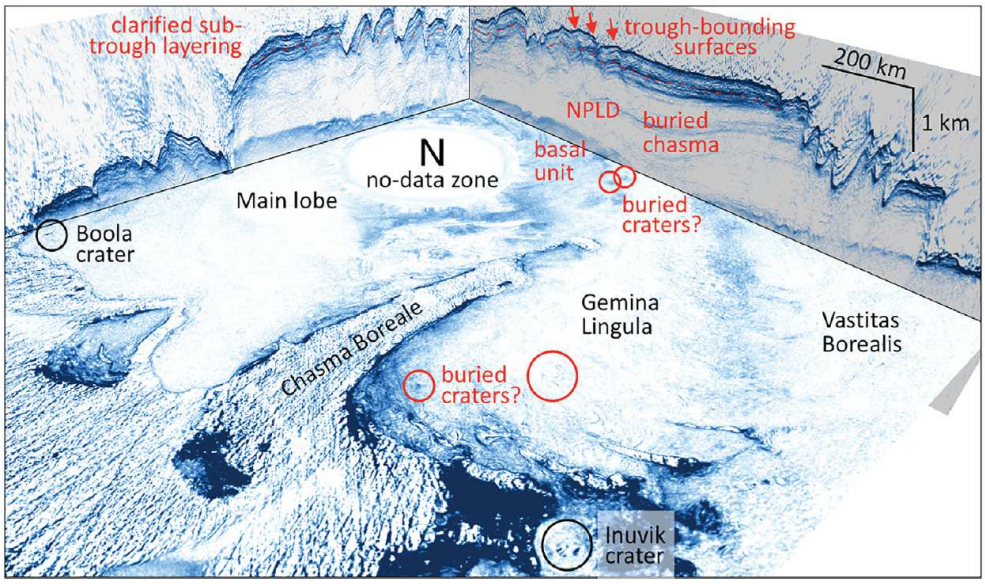

Figure 2: Perspective view into the depth-converted SHARAD 3-D volume of the North polar cap, made by Putzig, Smith, et al., 2018, showing radar-return power (blue high, white low) from previously known (black) and buried (red) features. Image Credit: Putzig, Smith, et al., 2018

During winter season, in both caps the temperature can go under 150 K (−120°C). Thanks to these conditions, the martian polar ice is more rigid and less plastic than it would be on Earth. Furthermore, the presence of dust layers and the weaker gravitational force on the surface of Mars, amounting only the 38% of the one exerted by the Earth, increase the resistance to flow of the martian ice sheets (Faure and Mensing, 2007). Nevertheless, the topographic profile of the north polar cap is *dome-shaped*, even if the low plasticity should counteract its development in this form and favor a flatter profile. Therefore, the martian ice sheets do appear to flow outward from their centers, where the ice is thicker than at the margins. The flow rate of the martian north polar ice cap is about 1 mm/yr, compared to rates of 1 to 10 m/yr, typical of terrestrial ice caps (Fishbaugh and Christine S Hvidberg, 2006).

Both caps present a spiral pattern, the *Spiraling Troughs* (visible in Figure 1), produced by roughly perpendicular katabatic winds, circulating because of the Coriolis Effect. These valleys spriral anticlockwise in the northern cap, clockwise in the southern one. This process produces canyon-like structures where part of the ice has melted and they allow a view of the cap inner stratification. In fact, from high-resolution images of the Spiraling Troughs, it is possible to see and study exposed parts of the PLD.

The PLD are also subject to *subsurface sounding radar analysis*, that allows the study of the parts which are not reachable from imaging instruments too. In fact, ice is relatively transparent to radar signal. This allows to study the deposits content of dust, which is distributed over layers that in part reflect radar signal (the mechanism is deepened in Chapter 4). In the North Polar Layered Deposits (NPLD), the attenuation of the radar signal, as a function of depht, permits to establish a maximum bulk dust content of 5% (Grima et al., 2009), while in the South Polar Layered Deposits (SPLD), the dust content was found to be around 10-15% (Seu et al., 2007).

Although the surfaces of the PLD are very flat and smooth, they are bounded by steep, *marginal scarps*, with slopes that exceed 10° and rarely reach 90°. Like the Spiraling Troughs, they typically expose up to a kilometer of vertical layering (Smith et al., 2020).

Martian polar caps seem to have very few *impact craters*, although, given their age, they should show many more. This could be due to the interaction between the ice sheets and the atmosphere and the obliteration caused by the flow of the ice. For

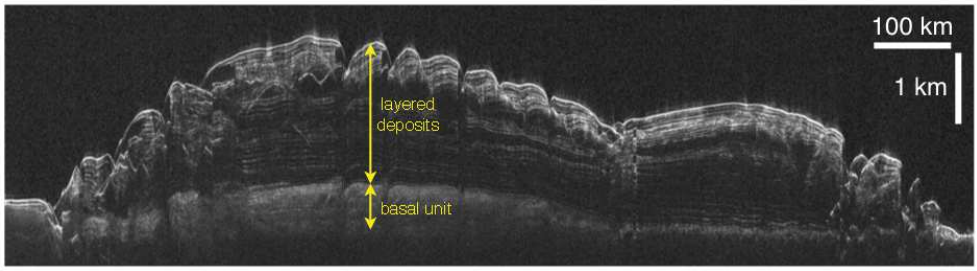

Figure 3: SHARAD radargram revealing NPLD overlying a basal unit in some areas. Image Credits: NASA

this reason, age estimation through crater densities is much more complicated in the caps regions, with respect to other terrains where impact craters are preserved for longer timescales. Therefore age estimations are also done through climatic and dust and ice deposition models.

Nevertheless, thanks to recent realization of three-dimensional volumes of both Martian polar caps, realized by Putzig, Smith, et al., 2018 with SHARAD radar data (a section is visible in Figure 2), it was possible to reveal several structures that seem to be *buried impact craters*, completely covered by the overlying layers of ice. These features provide a potential means to constrain the ages of both the substrate and the overlying icy deposits, that is independent of climate models.

2.2 NORTH POLAR CAP AND NORTH POLAR LAYERED DEPOSITS

The north polar cap is centered on the north-polar basin, whose elevation is close to $-5000\,\mathrm{m}$, and it rises about $3000\,\mathrm{m}$ from the surrounding plains (Faure and Mensing 2007). It has a diameter of $1000\,\mathrm{km}$ and a volume of $1.2 \pm 0.2\,10^6\ \mathrm{km}^3$ (Christine S Hvidberg 2004).

A particular feature that characterize the northern cap is the *Chasma Boreale*, a large canyon $500\,\mathrm{km}$ long, up to $100\,\mathrm{km}$ wide, and nearly $2\,\mathrm{km}$ deep, visible in the left panel of Figure 1 and labeled in 2. There are several hypothesis about its formation, like catastrophic outburst of water (Clifford, 1980), protracted basal melting (Greve, 2008), erosional undercutting (Edgett et al., 2003), aeolian downcutting (Warner and Farmer, 2008) or a combination of these processes (Fishbaugh and Head III, 2002), but the most accredited one is that it was a pre-existing feature, formed before the spiral troughs, and seemingly growing deeper as new ice deposits built up around it (Holt et al. 2010).

Another important component of this cap is the *Basal Unit (BU)*, highlighted in Figure 3. Revealed by high-resolution images, it has been found beneath the NPLD. It distinguishes itself from the NPLD principally thanks to its lower albedo, measurable in its exposed region along a few arcuate scarps, but also its thicker layers. This region, reaching a thickness of $\sim 1000\,\mathrm{m}$ beneath the highest portions of Planum Boreum[1], interposes between the NPLD and the Vastitas Borealis Formation, with the exception of the Gemini Lingula reagion, where the BU interrupts abruptly (Roger J Phillips et al., 2008).

Among all the regions that characterize the northern cap, in this work we will focus in particular on the NPLD (displayed in Figure 3 and 4). This region is particularly interesting because it contains the information about past climate conditions

1 i.e. The northern polar plain. Visible in the left panel of Figure 1 under the cap. It interfaces the Vastitas Borealis with a collection of mesas and troughs. The interface is visible in the aforementioned Figure, west of Chasma Boreale, and it consists in an irregular scarp, named *Rupes Tenuis*.

Figure 4: A section of NPLD captured by HiRISE instrument on Mars Reconnaissance Orbiter (MRO). Image Credit: NASA

on the planet. Each layer characteristics have been influenced by the atmospheric conditions of its formation period, including temperature, relative humidity, and aerosol dust content, along with atmospheric and isotopic materials (Smith et al., 2020).

According to climate models, NPLD should have developed in the last $\sim 5\,\mathrm{Myr}$ (Roger J Phillips et al. 2008), postdating the last transition from high to low mean obliquity. Before this moment, when the martian obliquity value could have been $> 40°$, the ice of the pole should have been unstable against complete loss by sublimation Jakosky et al., 1995. Thus, the age of these deposits should be less then $5\,\mathrm{Myr}$. This means that NPLD are younger with respect to the southern one and this makes them more suitable for our analysis for the reasons that are explained in the next Chapter 3. In fact SPLD are dated between 7-14 Myr Ken E Herkenhoff and Plaut 2000, and 30-100 Myr Koutnik et al. 2002.

3 ORBITAL FORCING

3.1 ORBITAL FORCING PHENOMENON

The alternating nature of the PLD structure is believed to be caused both by variations in the accumulation rates of ice and dust, and as a result of oscillations in Mars' orbital parameters. This last phenomenon is called *orbital forcing*. The variation of the orbital parameters affects the *insolation curve*, i.e. the flux of solar radiation per unit of horizontal area, for a given position on the planetary body, in function of time. The *insolation curve*, in its turn, influence the planet climate conditions.

In fact the *total flux* S (reported in Equation 1), received from the Sun, at the planet distance d, has a key role in the determination of the planet *temperature*.

$$S = \frac{L}{4\pi d^2} \tag{1}$$

Where L is the luminosity of the star. In the case of the Sun we have $L_\odot = 3.839 \cdot 10^{33}\ erg\, s^{-1}$.

Here we show the calculation of a planet *Effective Temperature* T_{eff}, in order to give an idea on how the insolation curve affect the climate. This parameter consists in the equilibrium temperature of a sphere, emitting like a black-body, located at a distance d from the Sun, of diameter r and albedo A. The albedo is the fraction of radiation that is reflected by the planet; it can vary from 0 (perfect black-body, all the radiation is absorbed) to 1 (totally reflective body). It is possible to obtain the value of T_{eff} through the equality between the portion of Sun flux absorbed from the planet, and the radiated energy, in the hypothesis that the planet thermal emission is the body-black one:

$$S(1-A)\pi r^2 = 4\pi r^2 \sigma T^4 \tag{2}$$

Where σ is the Stefan-Boltzmann constant. The equation 2 holds only for rapidly rotating bodies, otherwise the second member must by divided by 2 to take into account that the radiated energy comes principally form only one hemisphere.

The equation 2, among other things, does not consider the effect of the *atmosphere*. In fact, the atmosphere influences both the absorbed energy and the one radiated back to space. It can be opaque to a part of the received radiation, preventing it from reaching the planet surface, and it can absorb a portion of the energy thermally emitted by the ground, provoking the so-called greenhouse effect, which in turn warms the planet. Therefore, the effective temperature does not perfectly coincide with the planet real temperature, because of the many assumptions and simplifications that have been done, but it helps in the comprehension of the phenomenon.

The three orbital parameters (Figure 5) that influence the insolation curve are:

- *eccentricity*: it determines the amount by which the shape of an orbit deviates from a perfect circle. When its value varies between 0 (perfect circle) to 1, the orbit is elliptical. When it is equal to 1, or greater, it corresponds to parabolic or hyperbolic orbit, respectively.

  This parameter affects the insolation curve because it causes the distance between the planet and its star, d, to vary along the orbit. The annual variation

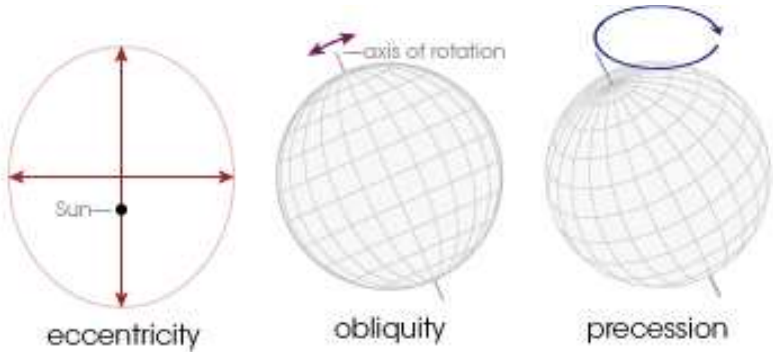

Figure 5: Three variables of the a planet's orbit, i.e. eccentricity, obliquity, and precession, that affect its climate.

in distance from the Sun, or the central star, leads to *"distance seasons"* which are synchronous between the hemispheres.

- *obliquity*: the angle between the planet's rotational axis and the axis perpendicular to the plane of its orbit.

  It influence the *strength* of the planet's *"obliquity seasons"*. This type of seasons is dominant for Earth and Mars, in contrast with their "distance seasons", and it produces effects which are out of phase between the hemispheres: while one experiments winter, the other experiments summer.

- *argument of pericenter*, or *argument of perihelion* in Mars case: the angle from the planet's *ascending node*, i.e. the point where the planet moves north through the plane of reference, to its *periapsis*, namely the point of minimum distance with the central body, measured in the direction of motion.

  The evolution of the argument of pericenter influence the timing of the planet's "obliquity seasons" and determines whether they constructively or destructively interfere with the "distance seasons".

All three change gradually on a scale of many thousands of years.

The evolution of the *argument of pericenter* depends on the *precession* phenomenon (schematically represented in Figure 5), namely when the axis of rotation of the planet is itself rotating about a second axis, because an *external torque* is applied to it. In this way the rotation axis starts to move describing a cone in the three-dimensional space. For planets, the torque can be provided by the slight deviations of the mass distribution from spherical symmetry, for instance by the equatorial bulge caused by rotation. Normally this is the major cause, but other asymmetries, including those due to the distribution of ice, and of major geographic features, can contribute (Pierrehumbert, 2010).

Obliquity variations arise instead from *fluctuations* in the torque on the planet, rather than the mean torque. The obliquity cycle is inextricably linked with the precessional cycle, which modulates the orientation of the aspherical planet with respect to the Sun, the planet's moons, if sufficiently massive, and all the other planets gravitational fields.

Finally, *eccentricity* changes in time because of the influence of other gravitational bodies in the system. In fact, the eccentricity value remains constant only in the two-body problem, consisting, in this case, of a planet and its star in isolation. Although the gravity of the Sun greatly dominates, the presence of other bodies induces perturbations on the planet's orbit and cause eccentricity to change gradually. Nevertheless, as shown by the *Lagrange-Laplace secular theory*, the *semi-major axis* remains nearly constant in the course of such eccentricity changes, reducing the climate impact of this parameter. In fact, if the semi-major axis remains the same over time, the *mean insolation* changes little even if eccentricity evolves, except for extremely non-circular orbits (Pierrehumbert, 2010).

3.1.1 Earth case

This bond between orbital dynamics and geology, on the Earth, is described by the so-called *Milankovich cycles*, which affect climate conditions, and therefore ice and sediment deposits.

The study of this phenomenon goes back to the late 1800s, when *James Croll* assumed that the *ice ages* were largely influenced by changes in insolation, due to variations in Earth's orbit and spin axis (Croll, 1867). He introduced the idea, supported by *Milankovitch* after him, whose name is now generally attached to the theory, that the main orbital parameters that affect insolation and its distribution were Earth's orbital eccentricity, obliquity, and precession, as previously explained (Section 3.1).

The amplitude of the *obliquity cycle* doesn't remain perfectly constant over time, but it's dominant period is on the order of 40 kyr. Its value varies narrowly in a range from about 22° to 24.5°. At present, the Earth is in the middle of its obliquity range. On the other side, *Earth's eccentricity* varies on a longer time scale of approximately 100kyr. However, there are also evidences, borne out by spectral analysis, of a 400kyr cycle of eccentricity, characterized by two high eccentricity cycles followed by two low eccentricity cycles. Instead, the precessional cycle has a periodicity of 22 kyr (Pierrehumbert, 2010). The evolution of this three parameters, in Earth case, is visible in Figure 6.

Milankivich's main contribution to the paleoclimatic field was to study the solar irradiance at different latitudes and seasons, in great mathematical detail, and to relate these calculation with planetary heat balance as determined by the planetary albedo and by reradiation in the infrared according to the Stefan's law (Berger, 1988), as described by Equation 2.

According to Milankovic's theory, ice ages should follow the precessional cycle. He was convinced that ice ages require the accumulation of snow on land, that is favored by mild summers, limiting melting of old snow and ice, and warmer, but still sub-freezing, winters, favoring snow accumulation, since the higher content of water in warmer air (Pierrehumbert, 2010).

Although some periodicities of climate changes have been observed and they appear to match the periods of orbital motions, Milankovich's theory results not totally confirmed yet. It is still unclear *how* orbital forcing influence the climate, because the model is not yet fully in agreement with all the observations. For example, in the last $600 - 650$ kyr, the main climate effect seem to have a 100 kyr periodicity, interpreted as the main ice-age rhythm and evident by the deep-sea sediment oxygen isotopic composition $\delta^{18}O$ (Shackleton, 2000). This isotopic information provide a measure of the Earth's water frozen in ice and, thus, a measure of Earth's global ice volume, typical of the relative sediments' formation period (Muller and MacDonald, 1997a). The 100 kyr periodicity, present from the mid-Pleistocene transition onward (from $\sim 0.8 - 0.6$ Myr ago, before that moment it was the 40 kyr period, relative to the obliquity variation, to dominate), is in phase with eccentricity variation, but of all the orbital cycles, accordingly to Milankovitch's theory, the eccentricity should have a significantly lower effect on the insolation, with respect to obliquity and precession. A probable explanation is that there are several contributions to the climate that complicate the system and make it much more difficult to recognize the individual contribution of the orbital forcing. For example, this 100 kyr periodicity is probably the response of the *global carbon cycle*, on which the eccentricity seem to have an immediate effect and causes changes in atmospheric carbon dioxide concentration (Shackleton, 2000).

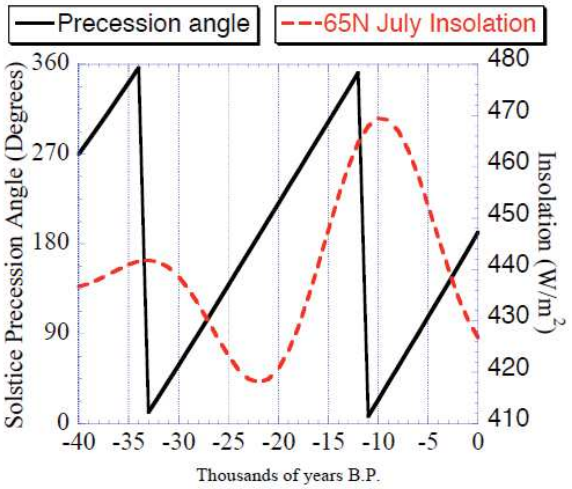

(a) *Evolution of precession angle relative to the Northern Hemisphere Summer Solstice, and the associated July insolation at 65°N. Graphic made by Pierrehumbert, 2010 with Berger and Loutre, 1991 data.*

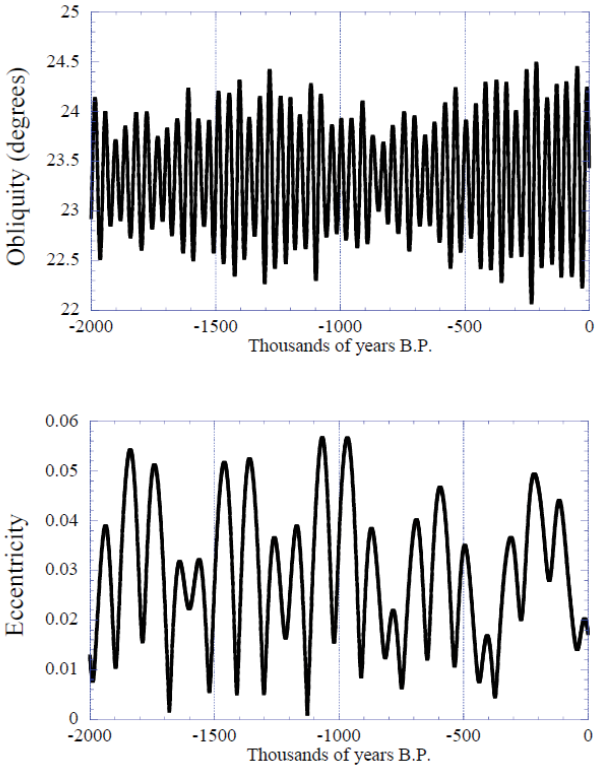

(b) *Evolution of the Earth's obliquity and eccentricity. Graphic made by Pierrehumbert, 2010 with Berger and Loutre, 1991 data.*

Figure 6: Evolution of Earth orbital parameters.

3.1.2 Mars case

On Earth, variations in the orbital and axial parameters are on the order of 2° and much smaller than those on Mars (Christine Schøtt Hvidberg et al., 2012). Furthermore the atmospheric system is much more complicated by the huge influence of the hydrosphere and the biosphere. For these reason, the study of the effects of the orbital forcing phenomenon could be more clear in Mars case.

Martian climate changes may have been caused principally by *obliquity variations*. In fact, an increase in the rotation axis' inclination allows more sunlight to reach the polar regions. In this way the rate of sublimation of CO_2 and water ices increases and causes the atmospheric pressure to rise, together with the greenhouse warming. Therefore, the climate of Mars may have fluctuated between cold and warm period in response to the cyclical obliquity variations. In this way, the global climate of Mars is controlled by its polar regions (Faure and Mensing, 2007). Obliquity has a *variation period* of 120 kyr and an *oscillation amplitude* of $\sim 10 - 15°$ about its mean value (Soare et al., 2018).

As the obliquity behavior is *strongly chaotic*, due to the proximity of secular spin orbit resonances (Laskar, Correia, et al., 2004), it is not possible to give a solution for its evolution over more than a few million years. In this context we find Laskar, Correia, et al., 2004 simulations (detailed in Section 3.2): they provided a precise solution for the evolution of *Mars spin* over the last 10 to 20 Myr. For this reason we decided to focus on the younger North polar cap, in order to correlate the known evolution of the orbital parameters with its structure. For the Southern cap, dated between 7-14 Myr Ken E Herkenhoff and Plaut 2000, and 30-100 Myr Koutnik et al. 2002, this study is complicated by the fact that there is no reliable climate function to compare to the SPLD record, as the solutions for the past orbital evolution of Mars are non-unique before ~ 20Myr (Laskar, Correia, et al., 2004).

As previously said, the structures that best record the climatic changes on Mars are the PLD. Studying the periodicity of their layering, it is possible to make a comparison with the typical timescale of variation of the orbital parameters. In order to implement this type of analysis, we will use SHARAD radar data (described in Chapter 4), in which the stratification is clearly visible. Then we will confront the obtained strata periodicities with the evolution of orbital parameters described by the Laskar, Correia, et al., 2004 simulations.

3.2 LASKAR SIMULATIONS

In Laskar, Correia, et al., 2004 it is possible to find the *precession* and *obliquity equations*, together with the discussion on the *stability of the solutions* with respect to the uncertainty of the parameters, in particular of the *initial precession rate*. As previously mentioned, a precise solution cannot be derived over more than 10 to 20 Myr, nevertheless the equations are integrated over 250 Myr anyway, in order to establish statistics on the possible variations of the obliquity over this time span.

Computing the equations for the evolution of precession and obliquity, in the case of Mars, it is possible to neglect the effect of its satellites. In fact, in the case for *Phobos and Deimos*, their averaged exerted torque is equal to zero (Laskar, 2004). This makes the equation simpler with respect to the Earth's ones.

Laskar, Correia, et al., 2004 assumes Mars as a homogeneous rigid body, with moments of inertia $A < B < C$, and with its spin axis coinciding also with the principal axis of greatest inertia.

Moreover, they considered some *dissipation effects*, like tidal dissipation due to the Sun, core–mantle friction, and climate friction. Actually, the effect of *solar tidal dissipation* is very small, as it amounts to less than 0.002° after 10 Myr. Consequently, the rotation rate of Mars did not change very much since the beginning of the Solar System. Instead, for *core–mantle friction* is meant the phenomenon for witch, because

of the different densities, the core and the mantle do not have the same *dynamical ellipticity* H[1]. This causes the two parts to precess differently around an axis perpendicular to the orbital plane, since the precession torques exerted by the Sun on Mars' core and mantle are proportional to H. From Laskar, Correia, et al., 2004 calculations, the core–mantle friction effect results of the same order of tidal effects or even weaker. Then, *climate friction* is a positive feedback process between obliquity variations and the resulting *redistribution of volatiles* at the planetary surface, affecting its dynamical ellipticity. This effect not only depends on the instantaneous value of the obliquity, but also on its dynamical evolution. In this case it has been neglected because of the comparison with its entity on the Earth, where the water/ice mass are one order of magnitude more massive, but it has not changed the Earth's obliquity by more than 0.01° per Myr during the severe recent Pliocene–Pleistocene glaciations (~ 0–3 Myr, Laskar, Robutel, et al., 2004). Furthermore, the volatile response to obliquity forcing and martian internal parameters, like density, elasticity, rigidity and viscosity, are still poorly constrained.

Since the motion of Mars' spin axis results chaotic (Touma and Wisdom, 1993), its evolution critically depends on its precise *initial conditions*. Laskar, Correia, et al., 2004 presents some numerical integrations assuming the values of initial obliquity and precession angle to vary up to 10 times the standard error, calculated by Folkner et al., 1997, demonstrating that, even in this case, the maximum difference with respect to the nominal solution is less than 0.001° after 10 Myr, and thus negligible over the considered timescale. In fact, the main source of uncertainty in the long term evolution of the obliquity of Mars is the *uncertainty in its initial precession rate*. For their simulation, Laskar, Correia, et al., 2004 used the precession constant[2] provided by Yoder et al., 2003, obtained thanks to *Mars Global Surveyor* data.

The results of Laskar, Correia, et al., 2004 simulations for the obliquity, eccentricity, and insolation in summer at the North pole are presented in Figure 7 and will be used for the following analysis.

1 Defined as the ratio of the difference between the polar (C) and mean equatorial (A) moments of inertia to the polar moment of inertia:

$$H \equiv \frac{C - A}{C}$$

2 Annual rate of precession of the equinoxes.

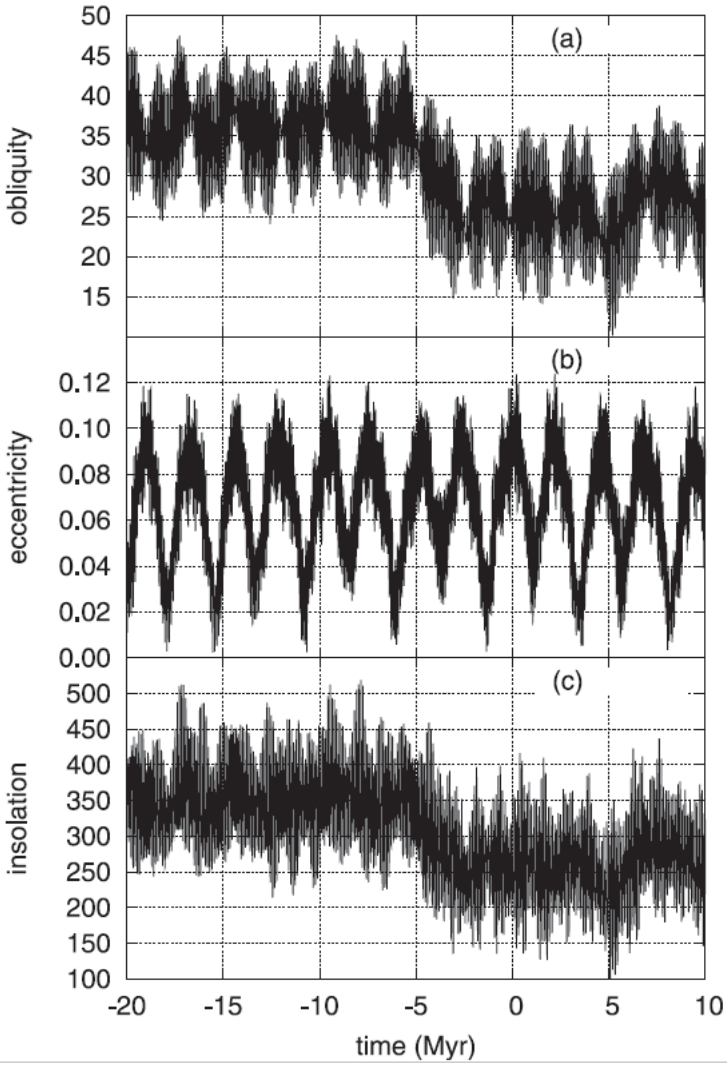

Figure 7: Obliquity (in degrees) (a), eccentricity (b), and insolation (c) (in watt m^2) evolution at the north pole surface at the summer solstice, during the period from 20 to +10 Myr.

4 SHARAD

4.1 MARS RECONNAISSANCE ORBITER MISSION

Mars Reconnaissance Orbiter (MRO) is a NASA mission, part of the *Mars Exploration Program (MEP)*. This Program has four main scientific objectives (Zurek and Smrekar, 2007):

- Search for evidences of past and present life.
- Study of Martian climate and volatile history.
- Study of geological processes and their influence in shaping the surface and subsurface of Mars.
- Evaluate the nature and available resources of the Planet, in preparation of human exploration.

MRO mission was launched on 12 August 2005 and successfully entered the Mars orbit on 10 Mars 2006. After finishing aerobraking, on 30 August 2006, the orbiter entered in its Primary Science Orbit (PSO), that was low-altitude ($\sim 300\,\mathrm{km}$), near-circular and near-polar (inclination of $i = 92,65°$).

On board there are six scientific instruments (schematically showed in Figure 9), including three imaging systems, a visible-near infrared spectrometer, a shallow-probing subsurface radar, and a thermal-infrared profiler. In this work we will use the radar data, in order to conduct our analysis.

4.2 SHALLOW RADAR (SHARAD) INSTRUMENT

4.2.1 Radar Technology

The term *Radar* is the acronym of Radio Detection and Ranging. It refers to those instruments that emit an electromagnetic signal toward a target of interest, and then

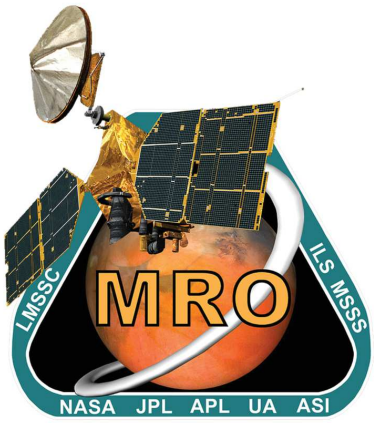

Figure 8: Mars Reconnaissance Orbiter mission logo.

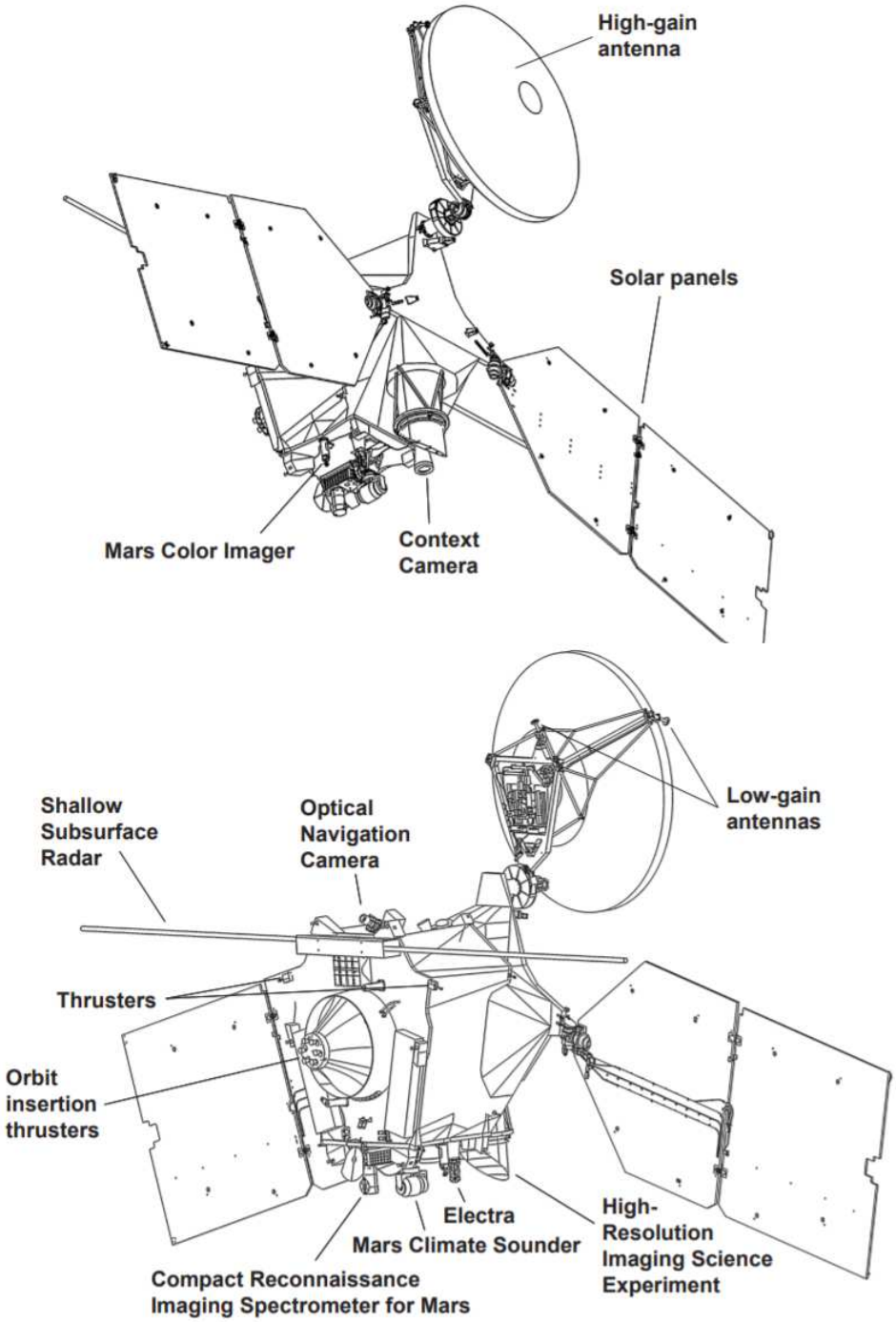

Figure 9: MRO spacecraft scheme. Image Credit: MRO Press Kit, 2006

they measure the characteristics of the returning signal scattered by the object, like the *intensity*, the *arrival time of the echo*, the *Doppler shift* and the *polarization*. Thanks to these information, it is possible to understand the *position*, the *velocity* and some *physical and geometrical characteristics* of the chosen target.

A typical radar consists of a transmitter, an antenna, a receiver, a signal processor, and a display. In the following only *monostatic* radar geometries will be consider, i.e. the *antenna* is used for both transmitting the signal and receiving the echo.

The radar emitted electromagnetic signal belongs to the frequency range spanning from *microwave* to *radio wave*. Each radar is therefore characterized by a *central frequency* f_c and a *bandwidth* B_w. These parameters determine the type of investigation of the instrument and thus its possible applications.

According to the waveforms transmitted, radars can be classified into *pulsed*, that transmit a relatively short burst of pulses, and after each pulse, the receiver is turned on to receive the echo, or *continuous-wave* radar, whose transmitter operates continuously.

The *intensity* of the emitted radar signal decreases with the square of the distance, and so also the diffuse ray. Consequently, the *echo intensity* diminishes with the fourth power of the distance between the radar and the selected target. This behaviour is evident in the general *Radar Equation* 3, describing the dependence of the received signal power P_r, from the transmitted power P_t, the antenna gain G, its equivalent area A, the target distance d and the radar cross section (RCS) σ:

$$P_r = \frac{P_t \cdot A \cdot \sigma \cdot G}{(4\pi d^2)^2} \tag{3}$$

Where the antenna equivalent area A depends on the antenna gain G and the wavelength of the signal λ, as described by equation 4.

$$A = \frac{G\lambda^2}{4\pi} \tag{4}$$

If we call S_{min} the minimum signal detectable by a radar, we can obtain an equation for the *maximum distance* R_{max} at which an object can still be detected:

$$R_{max} = \left(\frac{P_t \cdot A \cdot \sigma \cdot G}{S_{min} \cdot (4\pi)^2} \right)^{\frac{1}{4}} \tag{5}$$

Both P_r and R_{max} depend on the *radar cross section (RCS)*. This parameter is connected with the geometrical and physical properties of the target and it determines its radar detectability. It is the fictitious area intercepting that amount of power which, when scattered equally in all directions, produces an echo at the radar equal to the one received from the target (Chen, 2004). Mathematically, it fallows the equation 6.

$$\sigma = \lim_{d \to \infty} 4\pi d^2 \frac{|E_s|^2}{|E_i|^2} \tag{6}$$

Where:

- d is the distance between radar and target
- E_s is the scattered field strength at radar
- E_i is the incident field strength at target

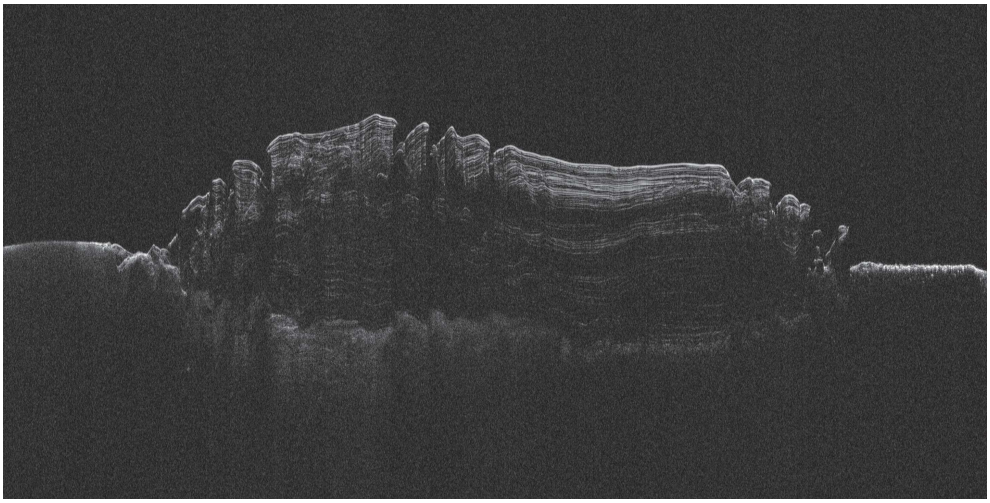

Figure 10: SHARAD radargram 00387302, showing a section of the NPLD.

Alternatively, the RCS can be expressed with another equation (7), in order to show its dependence from the target characteristics (Pettengill et al., 1962):

$$\sigma = \pi \cdot a^2 \cdot g \cdot r \tag{7}$$

Where a is the target radius, and thus $\pi \cdot a^2$ is the target geometrical section. g is a *directionality coefficient*, taking into account the irregularities of the object. It measures the amount of energy scattered back towards the radar, as compared to the average of that scattered in all directions. Finally r is the *radar brillance*, similar to the albedo concept in the visual spectral range: it is the target radio reflective power, connected with the *dielectric constant* ϵ of the material. For a perfect dielectric we have:

$$r = \frac{(1-\sqrt{\epsilon})^2}{(1+\sqrt{\epsilon})^2} \tag{8}$$

The *dielectric constant* ϵ, or *relative permittivity*, of a particular material, is the factor by which the electric field between the charges is decreased relative to vacuum. The tendency of a material to contrast an electric field affects the *speed* of an electromagnetic signal, like the one emitted by radars, passing through it. The value of ϵ is always greater then 1 and it can vary depending on the *temperature*.

An important aspect is that the radar signal can penetrate into the ground and reach materials with different dielectric constants. This makes possible the existence of *Radar Sounders*, which allow the investigation of the structural and dielectric characteristics of the subsurface, through a non-intrusive technique. They emit a sequence of short electromagnetic pulses, at variables frequencies, towards the ground. When the electromagnetic pulse, during his propagation, encounters a surface separating two materials, with different dielectric constant, part of the incident energy is reflected toward the surface, the other part continues its propagation in the deeper medium and makes possible other encounters and reflections on deeper discontinuity surfaces. The total amount of reflected energy, received back to the radar, is recorded as a function of *travel time* of the transmitted radar pulse and then used to compose the radar image, or *radargram*. These generated datasets are two-dimensional images that represent the *recorded echo power* for a given range position, as a function of the *horizontal distance* on the x-axis, and the *time*, or *depth* (if converted through formulas like 9), in the y-axis. In Figure 10 is showed a radargram captured by SHARAD instrument on MRO.

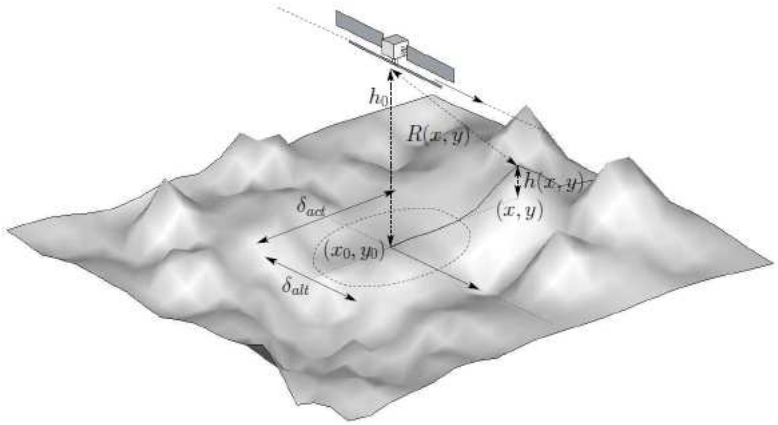

Figure 11: Acquisition geometry of a radar sounder instrument. The radar nadir point is denoted with (x_0, y_0). h_0 is the instrument height. δ_{alt} and δ_{act} are the along- and across-track resolutions on ground, respectively. The position of a generic ground point is denoted with (x, y) and its elevation is given by h(x, y). The distance between the radar and a ground point is denoted with R(x, y). Image Credit: Ferro, 2011

Knowing the composition of the materials crossed by the signal, it is possible to convert the time information of the y-axis, into a spatial one, using the Formula 9.

$$\Delta d = c\frac{\Delta t}{2\epsilon^{1/2}} \tag{9}$$

Another important application of radar technology, is the construction of high-resolution images of the underground, thanks to *Synthetic Aperture Radars (SAR)*. SAR are radars carried by a moving vehicle. In fact, as modern radar units are able to record hundreds of scans per second, a natural approach is data acquisition along lines. The antenna is moved horizontally while recording traces at fixed distances (Hugenschmidt, 2010). An example of the configuration is showed in Figure 11. The instrument can be mounted on a platform, like an airplane or a satellite, or a spacecraft, which flies at an altitude h_0 from the ground. The platform altitude depends on the mission profile and can span between several hundreds of meters and several hundreds of kilometers, depending on the type of platform (Ferro, 2011). At the beginning of defined Pulse Repetition Intervals (PRIs), the transmitter emits an electromagnetic pulse which travels from the radar to the surface and then penetrates the subsurface. SAR systems investigate an area using a *side-looking geometry*, explained in Figure 12. The radar beam is transmitted obliquely with respect to the nadir-direction, forming the *looking angle* θ with it, illuminating a *swath*, i.e. the radar footprint on the ground. This footprint can be approximated to an ellipse with a minor axis parallel to the *azimuth direction*[1], and the major axis in the perpendicular direction, called *range direction*. Synthetic aperture focusing can improve the along-track (azimuth) resolution without sacrificing the Signal to Noise Ratio (SNR) (Seu et al., 2007). Increasing synthetic aperture lengths, it is possible to obtain even finer azimuth resolution and reduce *surface clutter*.

Surface clutter is a phenomenon that affects radar sounding technologies. It consists in reflections from off-nadir surface features that produce lateral echos, appearing then in the range corresponding to the close subsurface, as they are recorded by the instrument at the same time of subsurface returns. This produces fictitious subsurface features in the resulting radargram. This problem can be solved with proper

1 The projection on the ground of the satellite flying direction.

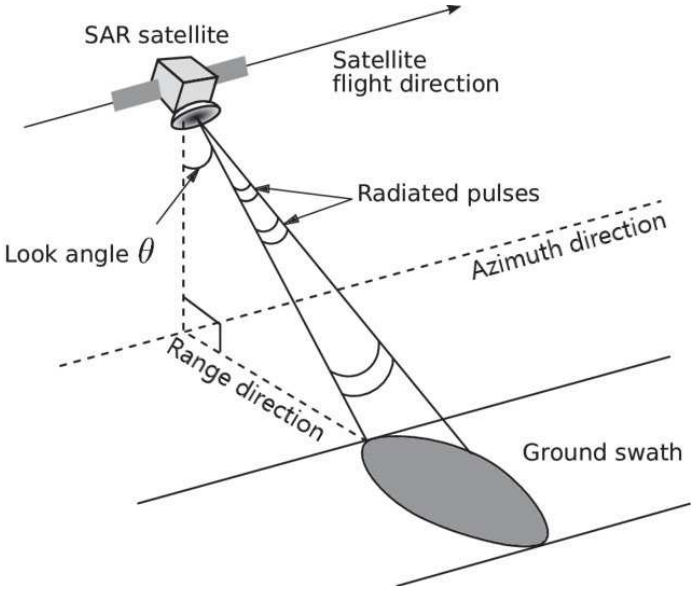

Figure 12: Simplified side-looking geometry of a synthetic aperture radar (SAR) system. Image Credits: Lauknes, 2011

simulations of surface echoes, obtained using Digital Elevation Models (DEM)[2], that can be subsequently removed by the data.

As *ice* is the most transparent material in the typical radar range of frequencies (Bogorodsky et al., 2012), spaceborne radar sounders have been used for the the study of other planets' or moons' poles or other regions of interest, where the presence of ice was suspected. Among them we find SHARAD, whose characteristics will be illustrated in the next section 4.2.2. Together with *Mars Advanced Radar for Subsurface and Ionosphere Sounding (MARSIS)*, on the ESA's Mars Express orbiter, it makes possible to reveal the *ice stratigraphy* of Mars' poles, and to detect *subsurface ice reservoirs* in other regions of the planet.

4.2.2 SHARAD

SHARAD is a wideband radar sounder, provided by the Agenzia Spaziale Italiana (ASI). It transmitts at a centre frequency of 20 MHz, thanks to a 10 m-long dipole antenna (visible in Figure 9). The bandwidth of the radar pulse is equal to 10 MHz and the pulse repetition frequency is equal to 700 Hz. It has a vertical resolution of $15\,\epsilon_r^{-1/2}$ m: 15 m in free space, finer in the subsurface, according to the properties of the materials crossed by the signal (Seu et al., 2007). The along-track resolution is equal to 0.3–1 km, narrowed by synthetic aperture processing on the ground, while the across-track one goes from 3 to 7 km, depending on surface roughness characteristics (Seu et al., 2007). Its altitude from the surface can vary between 255 and 320 km. For SHARAD, the same antenna transmits and receives the signals, with the spacecraft typically moving less than 10 m and *Doppler processing*[3] accounting for the relative motion between the spacecraft and the surface (Putzig, Smith, et al., 2018).

The main goal of SHARAD is to identify, in selected areas, dielectric interfaces to several hundred meters depth in the Martian subsurface. In this way, SHARAD

2 Digital representation of the distribution of altitudes in a certain territory. Each point of the area is associated with its height.

3 Relative motion between a signal source and a receiver produces shifts in the frequency of the received waveform. Measuring this Doppler shift provides an estimate of the relative radial velocity.

is able to search and map liquid or frozen water and study the occurrence and distribution of other expected materials.

In this work we decided to use SHARAD data because they give the possibility to visualize the layers underneath the polar surface in their entirety. In fact, the layering's periodicities quantification has already been made by Becerra, Sori, and Byrne, 2017, with the study of three different types of stratigraphic observations on imaging data: layer protrusion, local slope and layer brightness versus depth. This investigation is possible only where the layering emerges at the surface and becomes visible for imaging instruments. We want to extend this type of study inside the whole cap, using SHARAD radar sounder data. Furthermore, the analysis of *High Resolution Imaging Experiment (HiRISE)* images revealed a younger coating of dust and ice that modifies the visual appearance of exposed layers. This entails that the relation between the visual brightness of layers and their internal composition is not simple (Kenneth E Herkenhoff et al., 2007, Fishbaugh, Byrne, et al., 2010).

Moreover SHARAD has a much higher resolution with respect to its precursor MARSIS (~ 150 m in free space), making it more suitable to study the layering with greater precision.

4.3 SHARAD DATA

The design of SHARAD provides that the minimum amount of processing is done onboard. The onboard processing simply consists of coherent (with respect to the so-called Doppler bandwidth) summation of radar frames (Foss et al., 2017). The data are then focused onground through *range* and *Doppler focusing* of the chirp signals.

Raw data are processed at the *SHARAD Operations Center* of Thales Alenia Space (Rome, Italy), supervised by SHARAD science team. Data are then provided by the *ASI's Science Data Center* in Frascati, Italy[4], and by the *Geosciences Node of the Planetary Data System (PDS)* at Washington University in St. Louis, USA[5].

In this work we used the data processed by the *U.S. SHARAD team*, denoted as *MROSH_2001* and downloadable from `https://pds-geosciences.wustl.edu/missions/mro/sharad.htm`. They cover the period that goes from the 6th of December 2006, to the 8th of February 2020.

For each track, the archive reports:

- a *tabular geometric file* (*GEOM.TAB): an ASCII file reporting the important geographic, geometric, and phase-processing properties at each column of the radargram image. It is accompanied by a *label file* (*.LBL): an ASCII file that defines all the columns of its homonymous tabular file.
- a *a 32-bit raw image* (*RGRAM.IMG): the processed radargram image data. It is accompanied by a descriptive label file too, reporting its collection and processing parameters.
- a *full-resolution 8-bit TIFF* (*TIFF.TIF) version of the 32-bit radargram data. It is logarithmically scaled to a range of -3 dB to $+32$ dB with respect to the thermal background noise of the particular observation.
- a *reduced-resolution JPEG* (*THM.JPG) version of the 32-bit radargram data.

Thus, SHARAD radargrams are real-valued images of the radar backscatter power, arranged with time delay on the vertical axis and along-track samples on the horizontal axis. The along-track samples of each radargram are associated with latitude,

4 Available at: `http://www.asdc.asi.it`
5 Available at: `https://pds-geosciences.wustl.edu/`

longitude values in the homonymous GEOM file, which also provides information on spacecraft position and planetary radius for use in changing the reference spheroid surface.

All the passage that have been done to process the radargrams, before making them available for the scientific community, are detailed described by B. Campbell, 2014. The processing provides range compression, synthetic aperture radar processing, residual ionospheric time delays correction and datuming (Foss et al., 2017).

4.4 DATA SELECTION

In this section, we will explaine the process followed to select SHARAD data for our analysis.

The criteria we choose were:

1. Selected radargrams have to be equispaced over the whole north polar region.
2. Each selected radargram has to cover the entire length of the cap.

Firstly we describe the distribution of the data on the surface, in order to clarify the chosen selection process.

4.4.1 Data Distribution

As mentioned in Section 4.1, the spacecraft, on which SHARAD is mounted and takes the data, has a near-polar orbit, with an inclination of 92.65° with respect to Mars equatorial plane. This causes the existence of two "forbidden regions" that the MRO orbiter never flies over. Consequently, these zones are not covered by SHARAD tracks. They are centered on the two poles respectively, as we can see in the north polar case in Figure 13, upper panel.

Thanks to MRO flying configuration, SHARAD tracks are distributed densely near the no-data zones, and they tend to diverge going towards lower latitudes. In fact, as we can see in Figure 13, the Mid-Latitudes region, in the lower panel, results less covered with respect to the North polar region. Its percent coverage is equal to 38.39%, while the North polar one is equal to 90.51%. In the South (not present in the Figure but available at `https://sharad.psi.edu/maps/current_c_nadir.php#`) the percentage corresponds to 85.88%.

Given the high number of tracks in our region of interest, it is necessary to follow a selection process, explained in the next Section 4.4.2, in order to obtain a reduced number of radargrams suitable for our analysis.

4.4.2 Selection

In order to follow the criteria explained at the beginning of Section 4.4, we start with the consideration that, given the data geometry, every SHARAD track that intersects whole the cap must have a point in common with the contour of the no-data zone. In this point the track is approximately *tangent* to the circle that delimits this forbidden region.

As we wanted the data to be equally distributed along the cap, we select an *initial random point*, belonging to the circumference that surrounds the no-data zone, drawn in red in Figure 14, both in the upper panel, where we can see the distribution of SHARAD tracks (in blue) in the North polar region, and in the lower panel, zoomed on a particular region of the upper plot.

Then, defining a number N of radargrams that we want to analyze, it is possible to take N equally spaced point around the circumference (as we can see in Figure 14, upper panel, in black), differing of an angle equal to $\frac{2\pi}{N}$.

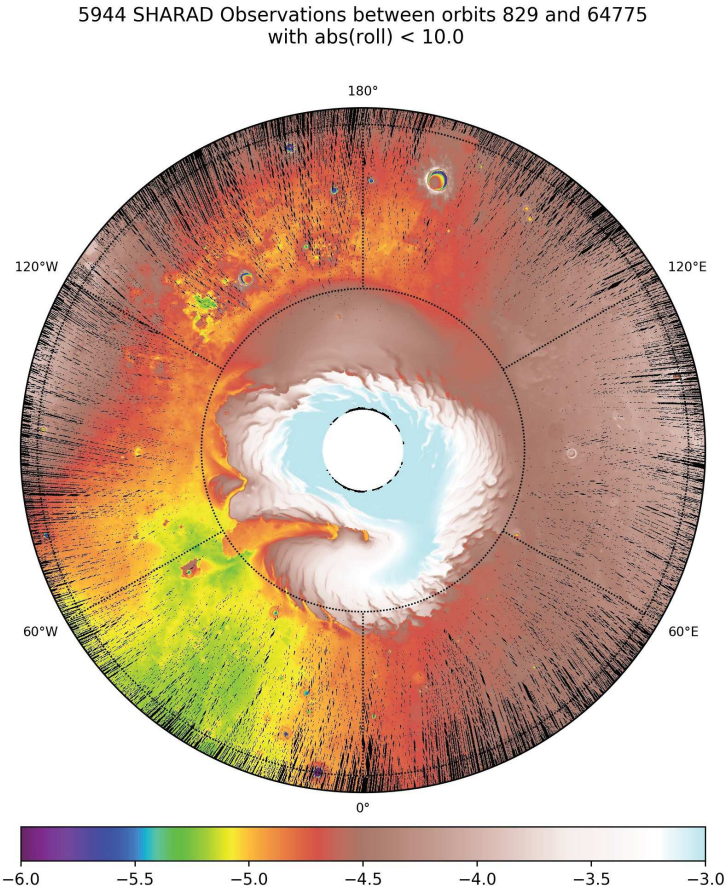

(a) *Coverage of SHARAD tracks in the North polar region (> 69°N). The percent coverage is 90.51%. It includes data taken until August 17, 2020. The no-data zone corresponds to the white central circle. Image Credit: The Planetary Science Institute*

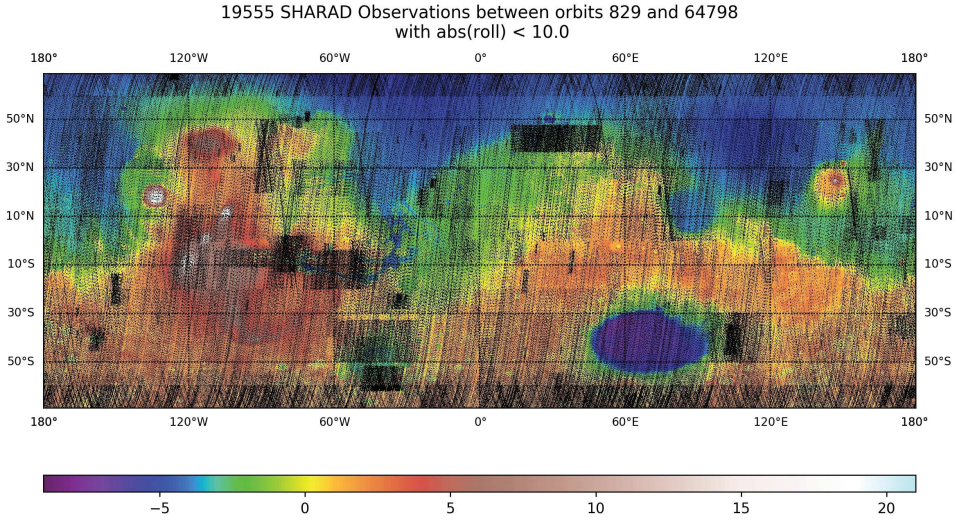

(b) *Coverage of SHARAD tracks in the Mid-Latitudes region (between 69°S and 69°N). The percent coverage is 38.39%. It includes data taken until August 17, 2020. Image Credit: The Planetary Science Institute.*

Figure 13: SHARAD tracks coverage.

We decided to take N = 10 because it was a good trade-off between a satisfactory data coverage of the cap, and the time that will be spent for the foreseen analysis of each radargram, because the proceeding, that will be explained in Chapter 5, is not completely automatic.

For each one of this point, we draw a circular sub-region centered on it. It is indicated in green in Figure 14, lower panel. In every sub-region passes a certain number of tracks, depending on the selected radius. We used for each sub-region a radius equal to 2000m. This choice is not particularly important because we only want to select a certain number of tracks, that will have approximately the same slope, and thus have the possibility to select, among them, the relative radargram in witch the stratification results more clear. Among all the tracks selected in a particular sub-region, we randomly selected three of them to check which one could be the more suitable for our analysis. This step is necessary because some radar images show blurred features, as we can see indicated by red arrows in Figure 15, probably caused by some technical issues during the acquisition phase, and in this way we can exclude them for the next analysis. The three randomly selected tracks for each sub-region are visible in Figure 16, upper panel.

At the end of this procedure we obtain the 10 radargrams (Figure 16, lower panel), one for each selection point and the relative sub-region, ready for the analysis that will be explained in Chapter 5.

4.4.3 3D Visualization

In order to better visualize the data, we made a *three-dimensional rendering*. This visualization is useful to see if it is possible to distinguish various unit inside the cap and how these units are distributed in the three-dimensional space. In particular seeing the data in this way, helped to confirm that the layering extends throughout the cap and, especially, that there is a particular unit, namely the one nearest to the polar surface, where the layers are more clear and evident.

The 3D visualization can be made selecting a region on the martian polar surface on *Q-GIS*[6], deciding a selection method to apply for the tracks that intersect the chosen region and making them visible in the three-dimensional space thanks to a Python module, called *Pyvista*[7].

Since we want our analysis to extend through the whole cap, the final region that we used was the one that include all the cap. The tracks that it includes are the one represented in Figure 14, upper panel.

A representation of the 3D is visible in Figure 17, 18 and 19.

6 It is a free and open-source desktop Geographic Information System (GIS) application. It is used for the visualization, editing, and analysis of geospatial data.

7 A Python helper module for the Visualization Toolkit (VTK), i.e. an open source software for manipulating and displaying scientific data. It allows to produce 3D plots, even with large/complex data geometries

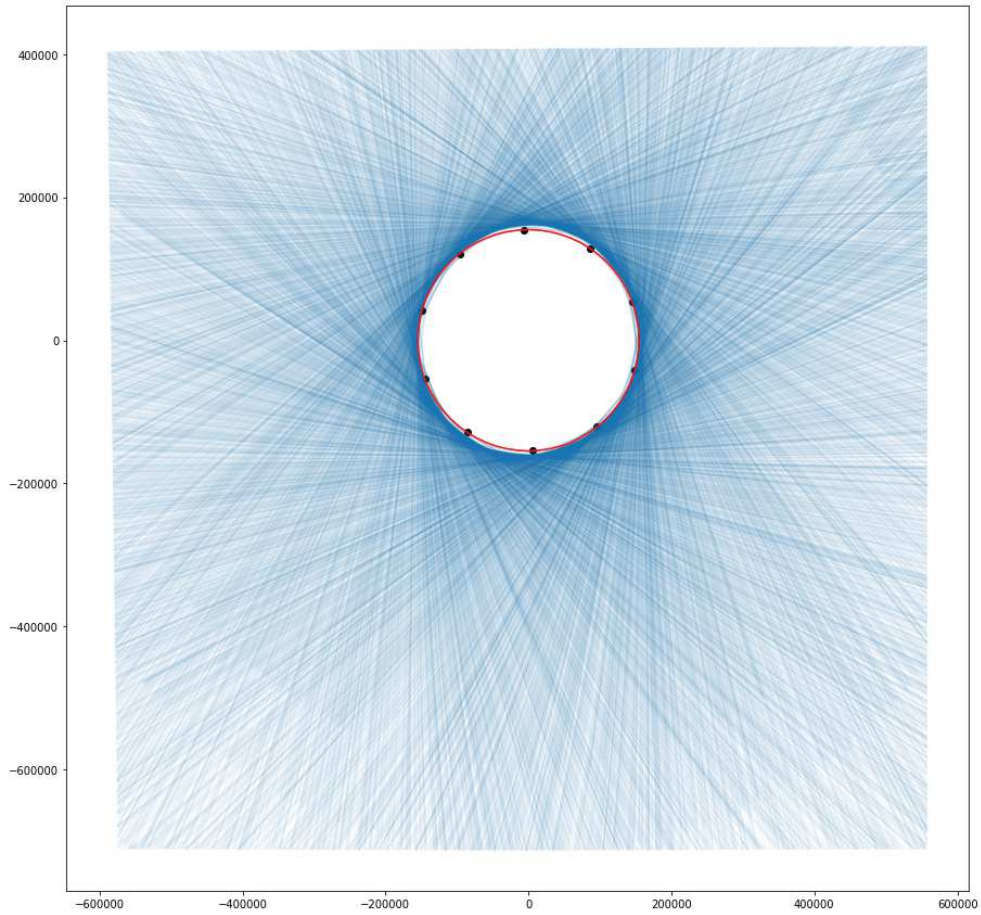

(a) *Distribution of SHARAD tracks (in blue) in the North polar region. In red it is plotted the circle that fits the contour the no data zone with the selection point in black.*

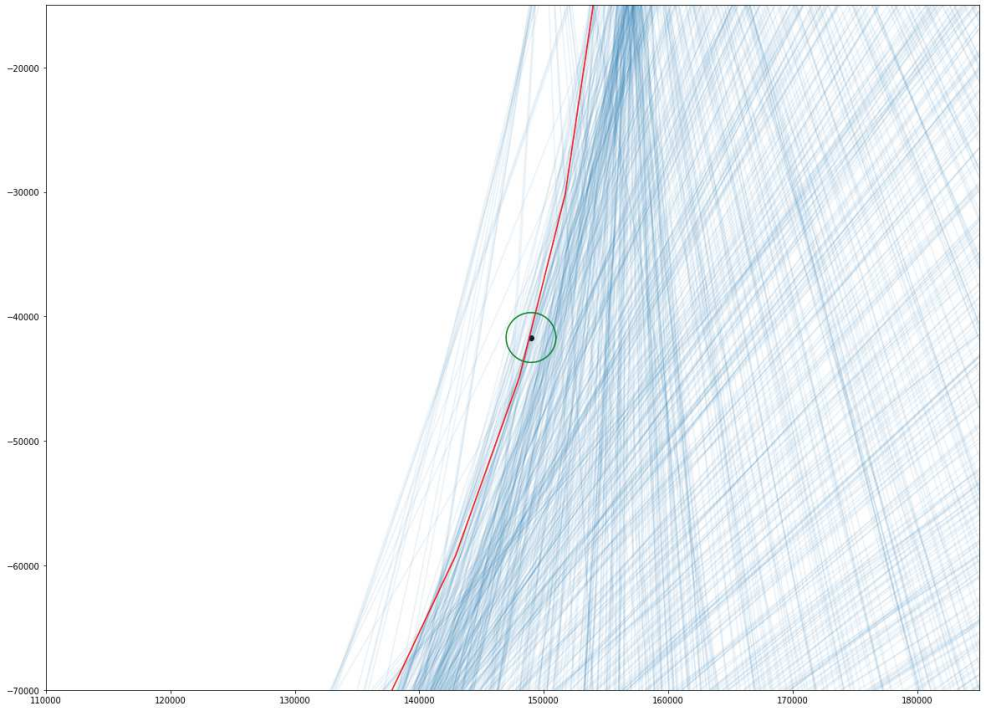

(b) *Zoomed region around one of the selection point in order to enlight the selection subregions delimitated by the green circle.*

Figure 14: SHARAD tracks in North polar region.

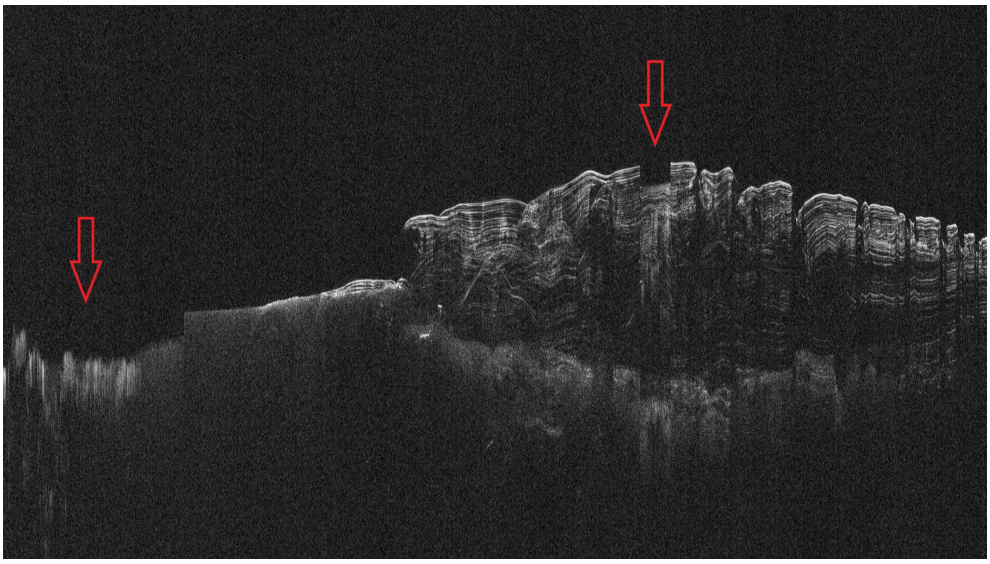

Figure 15: Example of damaged parts of a radargram, indicated by red arrows. It corresponds to SHARAD radargram 04254601.

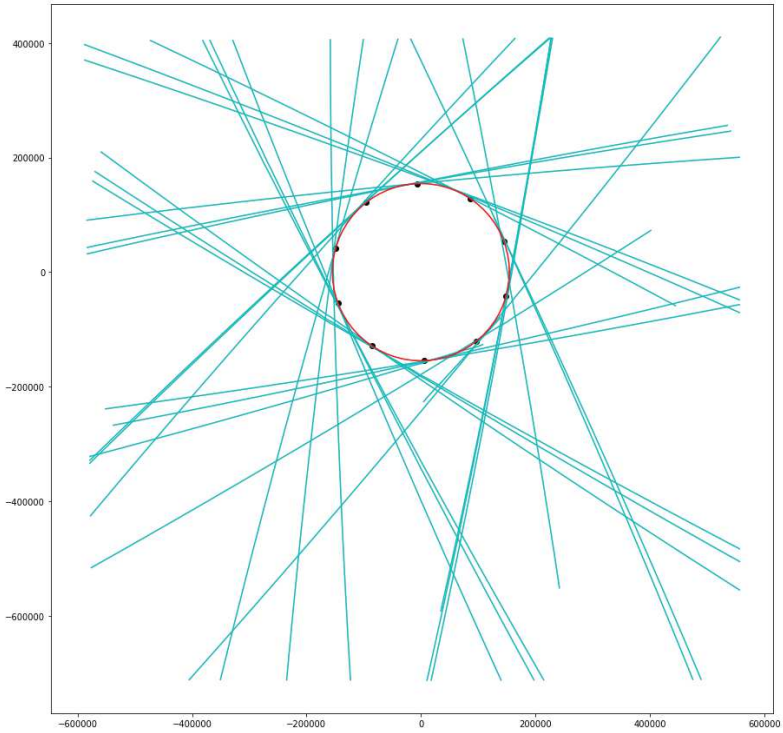

(a) *Distribution of the first selection of SHARAD tracks (light blue) in the North polar region. In red it is plotted the circle that fits the contour the no data zone with the selection point in black.*

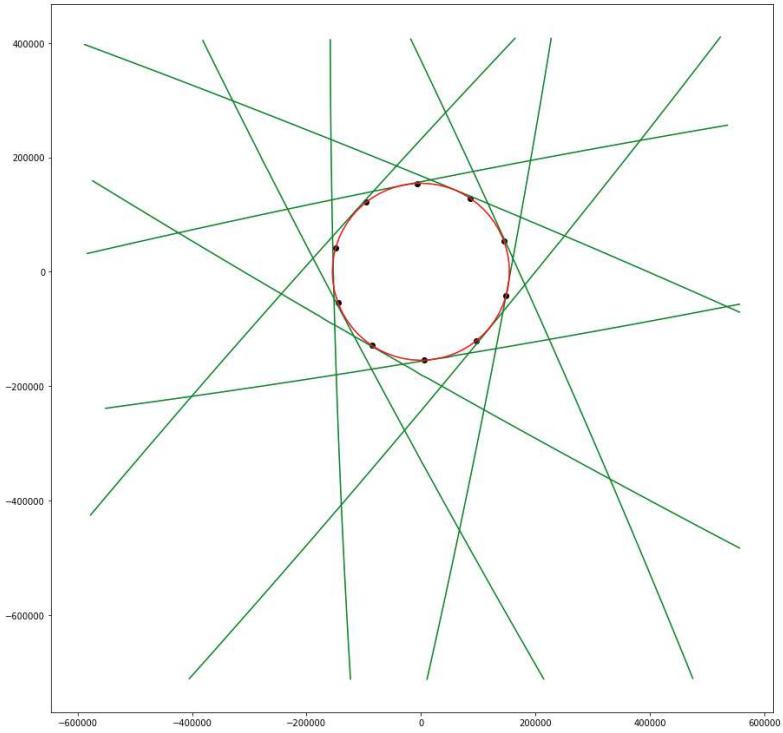

(b) *Distribution of the final selection of SHARAD tracks (green) in the North polar region. In red it is plotted the circle that fits the contour the no data zone with the selection point in black.*

Figure 16: Final SHARAD track selection.

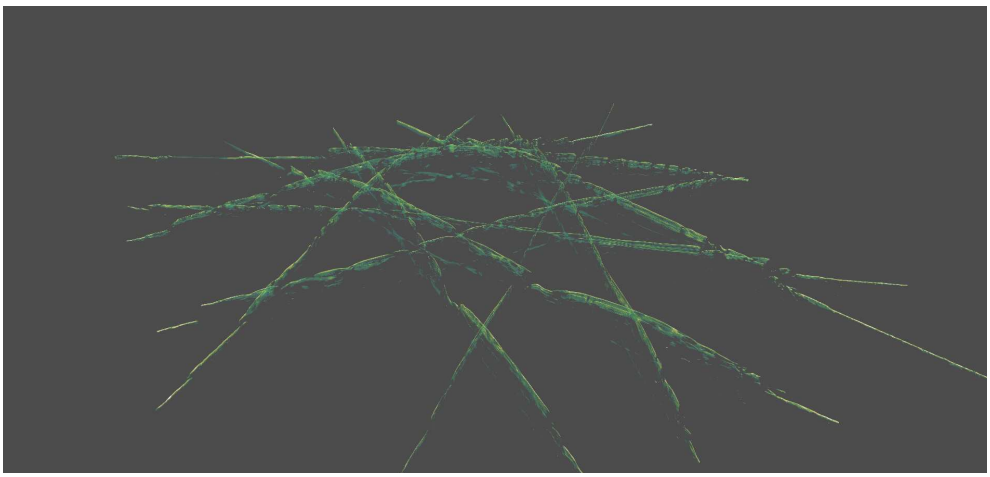

Figure 17: Snapshot of the 3D visualization of the selected tracks.

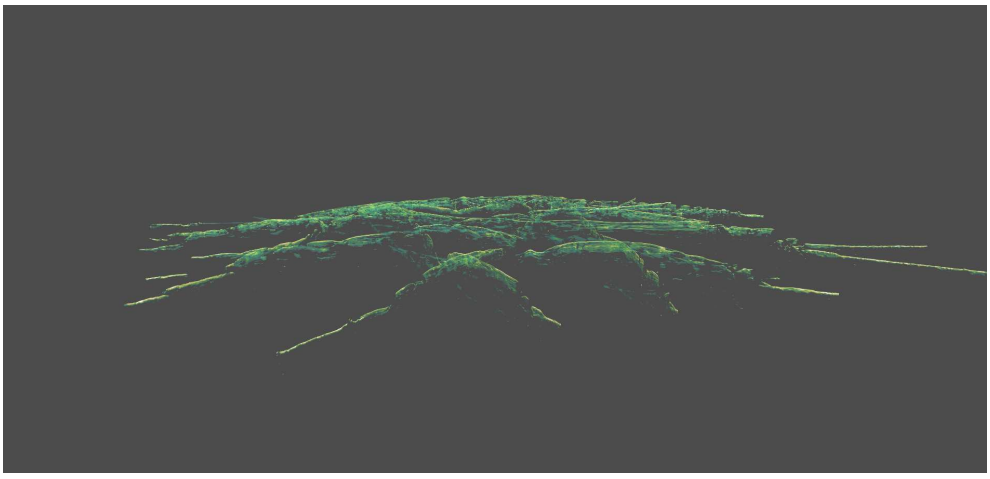

Figure 18: Snapshot of the 3D visualization of the selected tracks from a lower point of view, with respect to the Figure 17 one.

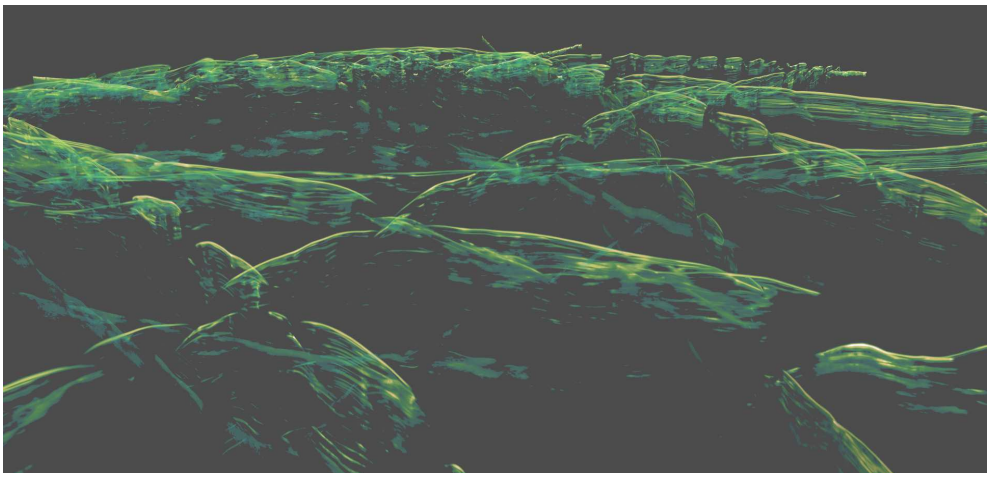

Figure 19: Snapshot of the 3D visualization of the selected tracks, zoomed toward the no-data zone.

5 METHODS

In order to extract the periodicities of the NPLD, we decided to concentrate on the areas of the radargrams where dense and strong scattering layering is present, i.e. the ones that appear evident both from the bi-dimensional radargrams, close to the polar surface (Figure 20, and from the three-dimensional visualization, mentioned in Section 4.4.3.

In the next sections we will explain the process followed to isolate these regions and to study the layering within them.

5.1 BACKGROUND NOISE CORRECTION

The fist step is to remove the *background noise* that characterized the images. It is particularly visible in the free space zone, over the cap (see Figure 21, upper panel).

There are several method to describe the *signal and noise statistical properties*. As demonstrated by Ferro, 2011, the *Rayleigh probability density function*, described by equation 10, can be considered the best fitting distribution for the no target areas, as the free space over the cap.

$$p_R(\xi) = \frac{2\xi}{\mu_{\xi^2}} \exp -\frac{\xi^2}{\mu_{\xi^2}} \tag{10}$$

Where ξ is the amplitude of the returns from a large number of independent scatterers, and thus ξ^2 indicates the signal power, while μ_{ξ^2} is the only parameter of the distribution and represents the mean power of the signal (Oliver and Quegan, 2004).

This means that the *background noise* of the SHARAD data can be modeled as a *zero mean Additive White Gaussian Noise (AWGN)* (Ferro, 2011). It describes the effect of many random processes that occur in nature. *Additive* means that it is added to any noise that might be intrinsic in the system. *White* refers to the fact that it affects all the system frequency band with the same entity. *Gaussian* because it has a normal distribution.

Among the various filters that can be used to remove this AWGN, we decided to use a *Non Local Means Denoising*, that consists in replacing the value of a pixel with an average of the values of similar pixels. These most similar pixels have no reason to be close to the first pixel taken into consideration. It is therefore licit to scan a more vast portion of the image in search of all the pixels that really resemble the pixel one wants to denoise, hence the definition "Non Local" (Buades et al., 2011). The portion of the image, used as a research zone for similar pixels, is limited to a square neighborhood of fixed size. We used a 21×21 window, as suggested by Buades et al., 2011. The result of the application of this filter is showed in Figure 21.

Besides the background noise correction, this filter has the additional effect to "smooth" the image and this affects the layering features in a way that will be useful for the later analysis. In fact it enhance the luminosity of the pixels present between two different successive layers, allowing an easier isolation of the regions of interest through a technique that will be explained in Section 5.3.

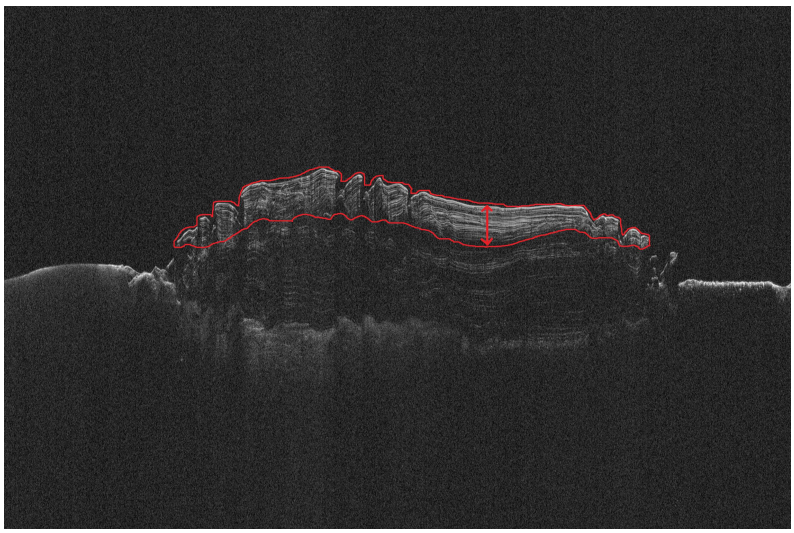

Figure 20: SHARAD radargram 00387302. Outlined in red it is possible to see the region where the layering is more evident.

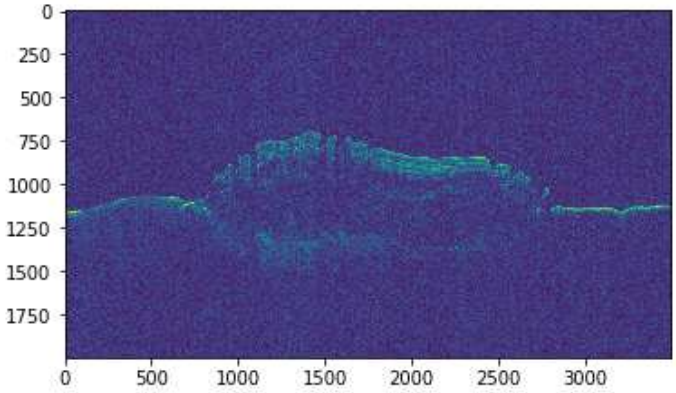

(a) *SHARAD radargram 00387302 before the background noise correction.*

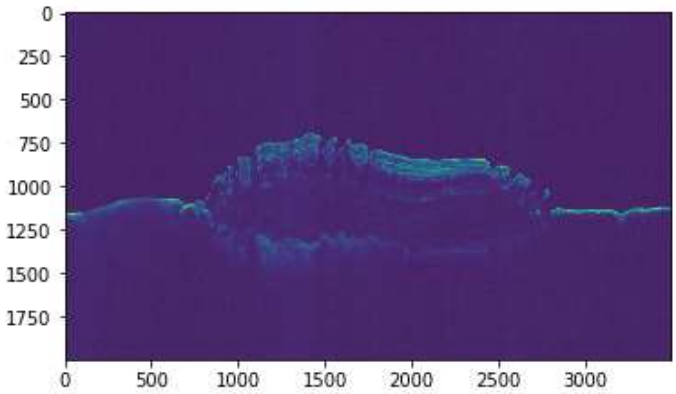

(b) *SHARAD radargram after the background noise correction.*

Figure 21: SHARAD radargram 00387302 before and after the background noise correction, through the Non Local Means Denoising.

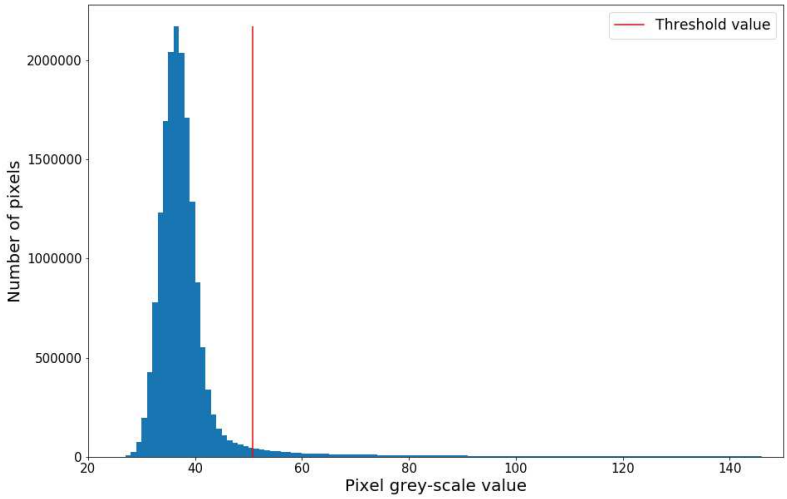

(a) *Histogram of SHARAD radargram 00387302, showing how many pixels have a particular gray-scale value. The red vertical line indicates the threshold value, equal to the value indicated by equation 11.*

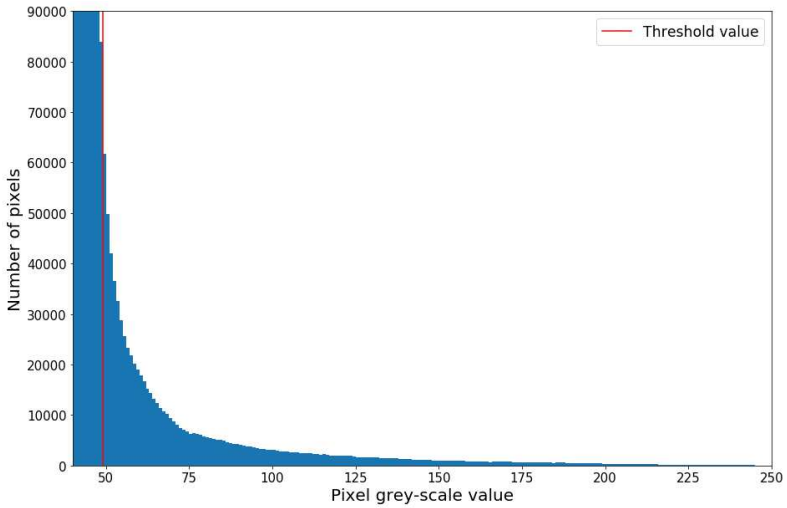

(b) *Zoom on the part of the histogram with the higher pixel grey-scale values. The red vertical line indicates the threshold value, equal to the value indicated by equation 11.*

Figure 22: Histogram of SHARAD radargram 00387302.

5.2 THRESHOLDING

With the purpose of isolating the region with the strongest layers, we apply a *threshold* on the radargrams. This operation consists in a partition of the digital images, in order to make them more suitable for our analysis. It transforms the radar images, which are *grey-scaled*, into *binary images*, where the pixels can only have values equal to 1 or 0. What discriminates the attribution of one value or the other is the *threshold value*, which can vary from 0 to 255 in the gray-scale. Pixels that have grey value greater then the threshold, become equal to 1, in the other case, they become equal to 0.

We decided to apply a threshold in order to extract the brighter part of the images, which comprises the higher layering region, and to make them suitable for the application of the method that will be explained in the next Section 5.3.

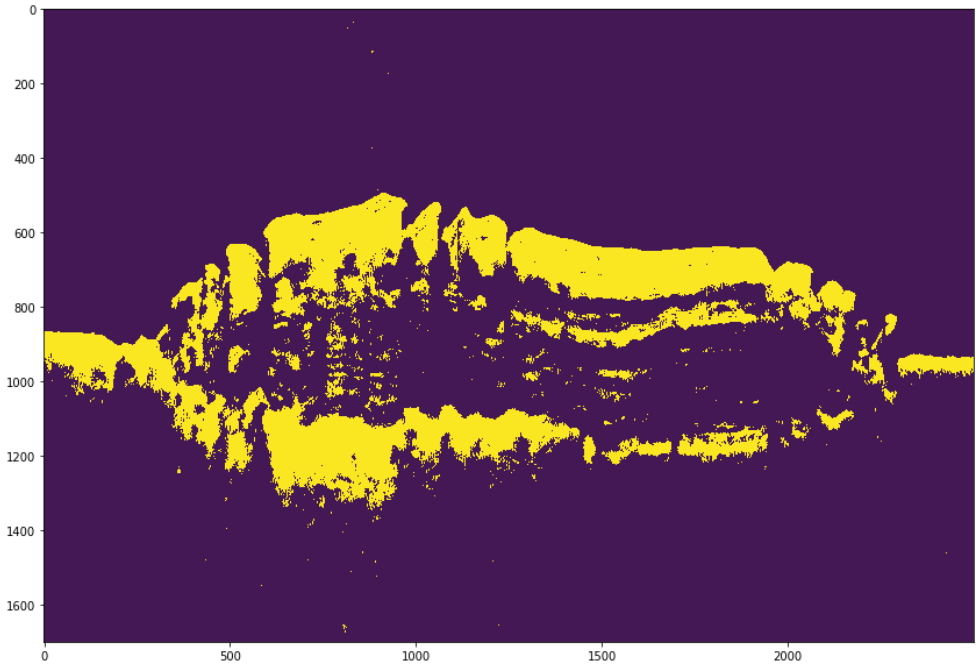

Figure 23: SHARAD radargram 00387302 after the thresholding. The pixels with value equal to 1 are represented in yellow, while the ones with value equal to 0 are represented in dark purple.

Given the distribution of the pixel values, visible in Figure 22, we decided to pick as the threshold value σ_{thr} the average of the pixels values $\bar{x}$ of the selected image, plus the variance $\mathrm{Var}(x)$, as indicated by equation 11.

$$\sigma_{thr} = \bar{x} + \mathrm{Var}(x) \tag{11}$$

This has the effect to select only the upper tail of the distribution that contains the brighter pixels. We can see the result of the threshold application in Figure 23.

5.3 LABELING OF CONNECTED COMPONENTS

The *Labeling of Connected Components* is a method to extract different regions of binary images. It consists in recognizing the components of the image where the pixels with value equal to 1 results connected with each other and, for each one of the found components, it gives a different label so as to distinguish them. In this way, a binary image is transformed into a symbolic image, in which to all pixels belonging to a specific connected component is assigned a unique label (He et al., 2009).

The *connection* concept derives from the relationship between pixels. It depends from the definitions of *neighborhood* and *adjacency*. Any pixel $p(x, y)$ has two *vertical* and two *horizontal neighbors*, specified by $[(x+1, y), (x-1, y), (x, y+1), (x, y-1)]$. A *4-neighbourhood* contains only these pixels. Instead a *8-neighbourhood* contains the same pixels and the four diagonal neighbors $[(x+1, y+1), (x+1, y-1), (x-1, y+1), (x-1, y-1)]$. The two type of neighborhood are showed in Figure 24.

In a binary image two pixels are *connected* if they are neighbors and they have the same value (0 or 1). This allows to define two type of connectivity, the *4-connectivity* or the *8-connectivity*, depending on the type of neighborhood.

Thus, the connected component algorithm starts by considering the first pixel of an image as the beginner of the first component. Then it recursively looks for

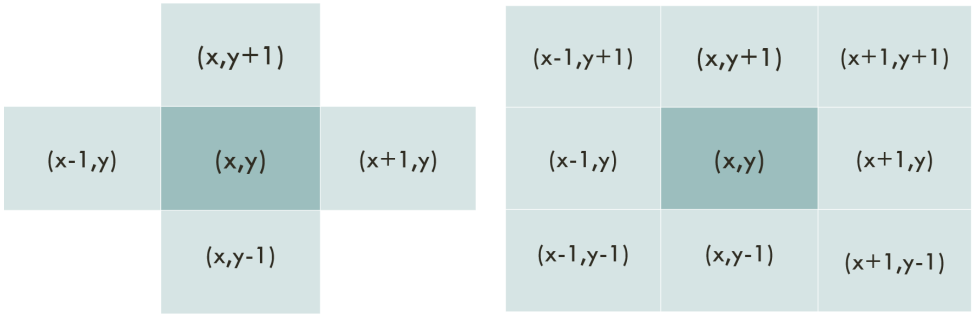

(a) *4-neighborhood representation for a central pixel with (x,y) coordinates.*

(b) *8-neighborhood representation for a central pixel with (x,y) coordinates.*

Figure 24: The two type of neighborhood relationship between pixels.

adjacent pixels, i.e. the one that are 4- or 8-connected to the considered pixel, in the binary image and adds them to this component. If no more connected pixels are found and if there are still pixels that have not been visited, a new component is initialized.

The result of the application of this technique to a radargram is showed in Figure 25. We chose a 8-connectivity criterion.

5.3.1 Connected Components Selection

As we can see in Figure 25, the connected component that corresponds to the region in which we are interested in, is the most extended. In other radargrams, it is possible that this region, with strong layering return, is divided into more than one connected component, maybe because of a small vertical discontinuity in the layering (i.e. open fractures or troughs in the polar cap) that is enhanced by the thresholding, but these are almost always the ones with the biggest area in pixels.

For this region, we decided to isolate the region by selecting only the components with the wider areas. Our automatic selection returns only the components with the pixel area greater than the average of all the areas of the connected components present in the image ($A_{px} > \bar{A}_{px}$). This criterion works efficiently in the images where the stratification is very clear and coherent over the entire length of the cap section. But if the layering shows many vertical discontinuities, it provokes several different components of smaller areas, that can be excluded from selection. Furthermore some images have a strong bright return even from the deepest part, where the cap rests on the terrain below and we can see distinguish the basal unit, and this might cause very wide components even where there is no layering. For this reasons we added the possibility to interact with the selecting program after seeing its fist output, so as to improve this step. For example, it can be inserted a certain number n determining how many times add or remove the standard deviation to the mean area value, in order to rise or lower the area value that determines the selection of the components ($A_{px} > \bar{A}_{px} + n \cdot \sigma_{A_{px}}$, where n determines the addition or the subtraction, if it is set as a negative value). When it rises the program selects less components of bigger areas, in the other case, it selects more components, with some less extended. Another possibility is to change the threshold value (σ_{thr}, previously defined in equation 11), adding or removing m-times the variance to the initially set value ($\sigma_{thr} = \bar{x} + m \cdot \mathrm{Var}(x)$). Changing the threshold allows to redefine the margins of the components. This can solve some discontinuity in the layering, if, lowering the threshold, some darker pixels that connect two distinct but close components become greater in value then the new σ_{thr}. In this way we obtain a new wider component that includes the previous two. Otherwise, it can happen that a selected component, corresponding to a bright region underneath the cap base in which we are not interested on, includes pixels whose values are higher

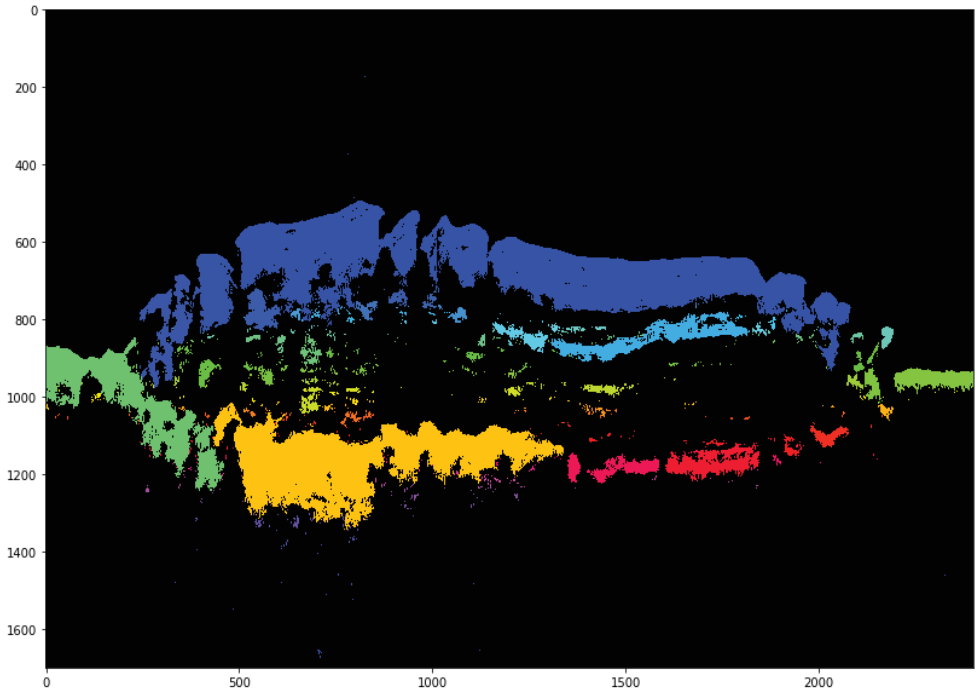

Figure 25: SHARAD radargram 00387302 after the application of labeling of connected components, with a 8-connectivity criterion. Each found component is reported with a different color.

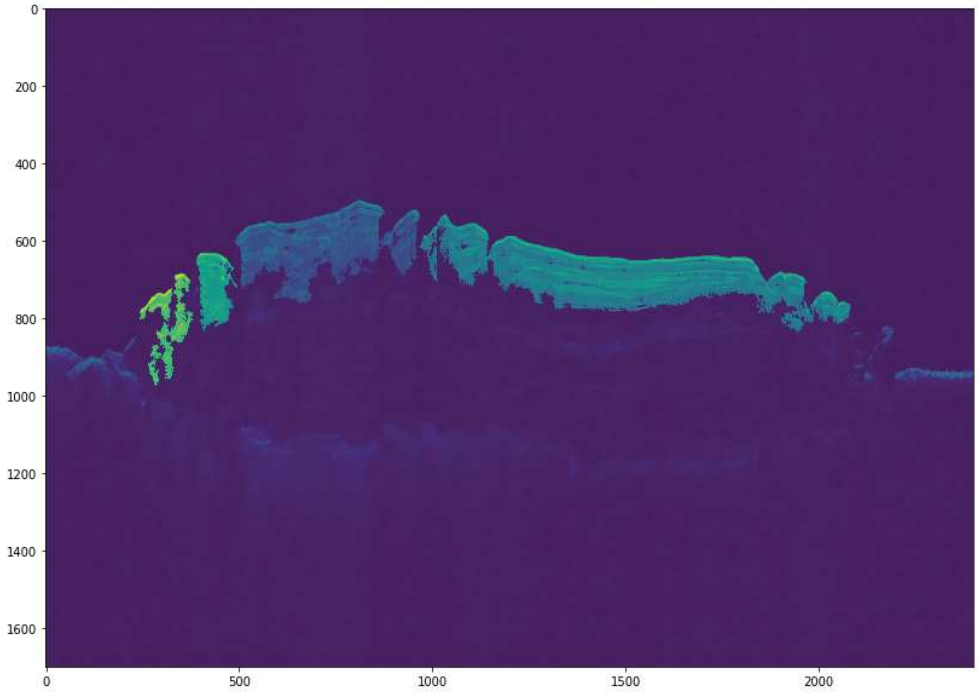

Figure 26: Final selected components for SHARAD radargram 00387302 highlighted over the original image.

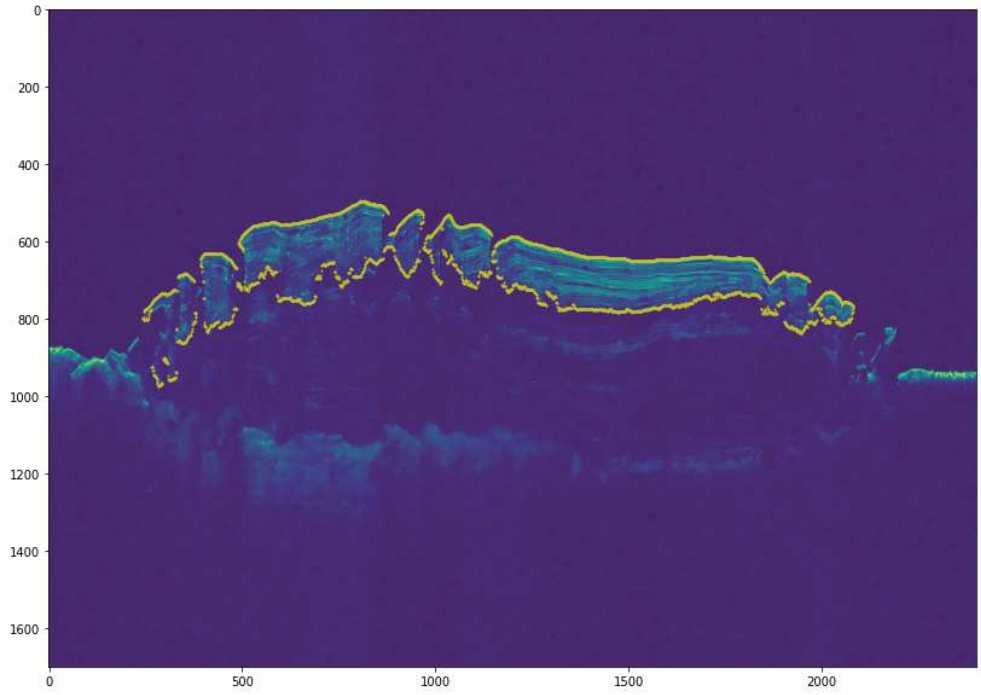

Figure 27: SHARAD radargram 00387302 with the points that delimit the selected components printed in yellow.

with respect to σ_{thr}, but lower with respect to the values of the pixels in our region of interest. Enhancing σ_{thr} can help to exclude the undesired component, while maintaining those that cover the region of interest.

However, when changing both the threshold and the area limits didn't produce the desired result, we added the option to make the decision, for every component of the image, to maintain or to remove that component from the final selection.

An example of the final result for the selection phase is visible in Figure 26.

Then we extracted the points that delimit the selected components, so as to obtain the contour of the region of interest. The delimiting points are showed in yellow in Figure 27.

5.4 THICKNESS DERIVATION

At this point we decided to make an evaluation of the *thickness* of the region, where the layering signal is particularly intense.

This step is possible because we isolated a region where it is possible to assume a *mean dielectric value*. In fact, the radargrams y-axis is in time unit, reporting the time interval that the radar signal takes to reach the reflective surface and come back to the detector. For a complete conversion into spatial units it is necessary to segment the image into different zones with similar composition and, thus, dielectric constant value, for example the free space over the cap, the cap itself and the surrounding and underlying terrains.

For this selected part of the image, we used the same dielectric value as the one assumed by Putzig, Roger J Phillips, et al., 2009, i.e. $\epsilon = 3.15$, typical of pure water ice under Martian surface conditions (Grima et al., 2009). This ϵ value was then substitute inside equation 9.

In order to obtain the thickness value Δd for each column of the region, we calculated the thickness in terms of pixels Δpx, as the difference between the y-coordinate of the two delimiting points (highlighted in yellow in Figure 27) present in that column. Then we used the *conversion factor*, provided by the U.S. SHARAD

team (B. Campbell and R. Phillips, 2014), to convert Δpx into Δt. The conversion is showed by equation 12.

$$\Delta t = 0.0375 \cdot 10^{-6} \Delta px \tag{12}$$

In this way it is possible to deduce that, inside the cap, and thus in the considered region, $1\,px \simeq 3\,m$.

5.5 TIME SERIES ANALYSIS

A *time series* is a collection of numerical observations arranged in a particular order. Normally they are a function of the *time*, that allows to establish a sequence in these observations (Bloomfield, 2004).

In this contest, *Fourier analysis* is a powerful instrument to study the behaviour of the system which generates these time series. It consist in the decomposition of a time series into a sum of sinusoidal terms. The coefficient of these terms are provided by the *Discrete Fourier Transform (DFT)* of the series. This Transform allows to represent the function in the *frequency domain*. In fact, it is possible to write the function that describes the behaviour of a signal in function of time $f(t)$ using a vector x formed by N samples of the signal, sampled with step τ:

$$x = [x(0), \dots, x(N-1)] \quad \text{with} \quad x(n) = f(n\tau) \quad \text{and} \quad n = 0, \dots, N-1 \tag{13}$$

It describes the information contained in the signal for that finite interval of time.

Then it is necessary to consider the other vector X, formed by N samples of the discrete time transform $X(\Omega)$, sampled with step $\frac{2\pi}{N}$:

$$X = [X(0), \dots, X(N-1)] \quad \text{with} \quad X(k) = X\left(\frac{2\pi}{N}k\right) \quad \text{and} \quad k = 0, \dots, N-1 \tag{14}$$

Where it is denoted with the same variable the vector $X(k)$, that represents the DFT, and the complex function representing the Fourier transform a discrete time $X(\Omega)$. Under the hypothesis that the signal energy is essentially contained in the N samples $x(0), \dots, x(N-1)$, we can obtain a formula for the DFT:

$$X\left(\frac{2\pi}{N}k\right) = \sum_{n=-\infty}^{+\infty} x(n) e^{-i\frac{2\pi}{n}kn} \approx \sum_{n=0}^{N-1} x(n) e^{-i\frac{2\pi}{n}kn} = X(k) \tag{15}$$

The DFT can be used for the *spectral analysis* of the signal, i.e. the representation of the signal in its *frequency* components. The aim of this method is to obtain the *spectral density*, or the *power spectral density*, that describes how the power of the signal is distributed over frequency. This helps to understand which frequencies are the ones that influence more the signal.

Since we are interested in the frequencies that characterize the layering, we decided to estimate their spectral density, to obtain the most significant ones.

We considered every pixels column of the selected region in the radar image as a time series, where the observations are the measurements of the reflected radar echo, which varies going deeper into the cap. Thus, from every column we can obtain a curve that represent the signal intensity in function of increasing time-delay measurements of the received signal.

Then each one of these time series is plotted, a little shifted in the x-axis direction, in order to obtain a *wiggle plot*. This type of plot is often used to visualize seismic

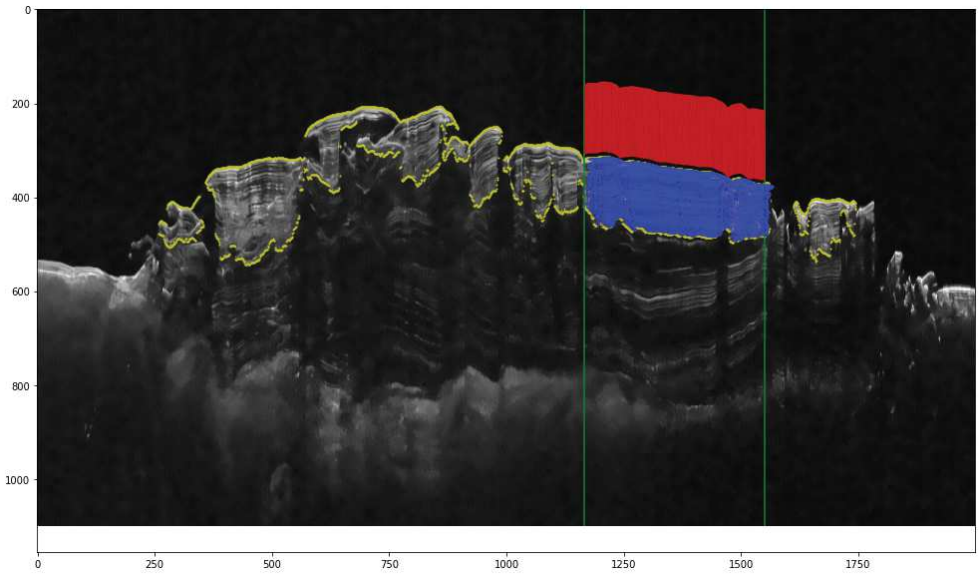

Figure 28: SHARAD radargram 01373502. The points in yellow delimits the region of interest, delimited through the labeling of connected components, explained in Section 5.3. Two green vertical lines delimit the restricted area that will be used for the spectral analysis. In blue it is highlighted the restricted area where are present the column selected for the wiggle plot (Figure 29), while in red is reported a region in the free space that will be used for the evaluation of the noise.

data. It helps to visualize the layers. In fact, one expects to find a peak in the echo power in correspondence of each layer and this should happen along the whole extension of the layer, creating a series of peak at a similar y-coordinate in the following curves shifted along the x-axis, so that these result aligned and delineate the reflective surface. For this reason, we decided to chose a restricted area of the previously isolated region, where the strata resulted more continuous, clear and extended, in order to obtain clear wiggle plots and to extract the periodicities. The resulting wiggle plot of the restricted area, highlighted in blue in Figure 28 for one of the radargrams and obtained with the selection explained in Section 4.4.2, is reported in Figure 29.

5.5.1 Periodograms

A *periodogram* is a method to obtain the *significative frequencies* that characterize a signal, because it allows to calculate the signal *spectral density* (Schuster, 1898). It acts by Fourier transforming a time-sampled data, and, by calculating the module squared of the transform, it obtains its energy spectral density. Then, by averaging the duration of the observation, it is possible to pass to the power density.

Before generating these periodograms relative to our region of interest, there are some operations that needs to be done in order to prepare the data.

The first step is to apply a *windowing function* on the signal, improving its spectral characteristics. Since we are working with finite-length signal, there is the possibility that it doesn't contain a integer number of periods, causing *truncated waveform*. When the number of periods in the acquisition is not an integer, the endpoints result discontinuous. This translates into high-frequency components in the Fourier Transform, that were not present in the original signal. This causes the energy at one frequency to leak into other frequencies, causing the so-called *spectral leakage*. This means that the spectral power is incorrectly estimated, so the results exhibit bias. The bias of the periodogram means that power at expected spectral peaks is slightly underestimated and the leaked power raises the spectrum elsewhere (Percival, Walden, et al., 1993). The spectral lines then appear wider then they would be

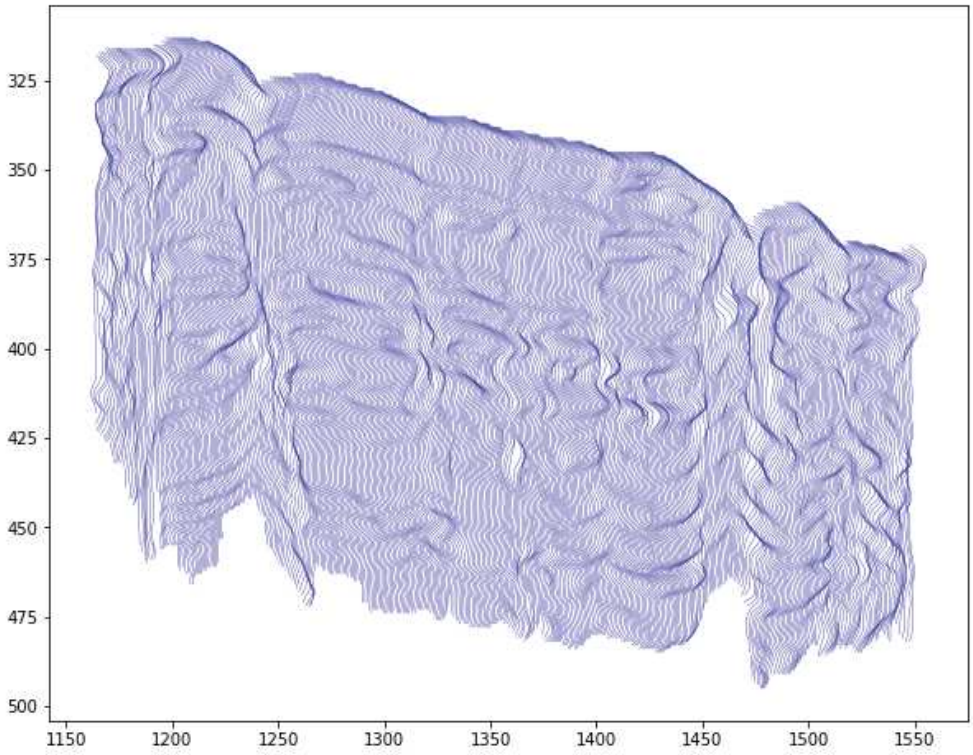

Figure 29: Wiggle plot for the time series extracted from the columns of the region highlighted in blue in Figure 28.

with an integer number of periods repeating inside the signal. Windowing is then a useful instrument to reduce the amplitude of the discontinuities at the boundaries of each finite sequence (Weedon, 2003). It works by multiplying the time record by a function of finite length, a *smoothing window*, whose amplitude varies smoothly and gradually towards zero at the edges. In this way, the resulting product is also zero-valued outside the interval. We choose a *Hamming window*, a taper formed by using a raised cosine with non-zero endpoints, optimized to minimize the nearest side lobe (Kanasewich, 1981).

Then we decide to *detrend* the time series, subtracting the *linear trend* from the signal. This allows to remove from the final spectrum some information in which we are not interested in. For example it removes the effect due to the natural decrease of the signal going deeper into the cap, that would cause the spectrum zero frequency, not useful for our analysis.

Subsequently, we make a *zero-padding* of the data. It consist in the addition of a certain number of zeros to each column, in order to increase their length up to reach an equal extension for all of them. In this way the signal is increased fictitiously and all the column can be easily mediated because of the same extension. This step allows to obtain a higher frequency resolution, narrowing the spectral lines (Muller and MacDonald, 1997b).

Finally, we used every elaborated time series to obtain a periodogram and then averaged all the obtained periodograms to get a unique one for each image (an example is showed in Figure 30).

In order to have an estimate of the residual atmospheric and instrumental noise, we apply the same process to the time series obtained in a region of the free space, over the selected region, highlighted in red in Figure 28. The resulting mean periodogram is plotted in blue in Figure 30 and it seem to give a very small spectral contribute. We amplified it in order to get an idea of its shape and to see which features could provoke on the signal spectrum. The amplified version is reported in green in Figure 30.

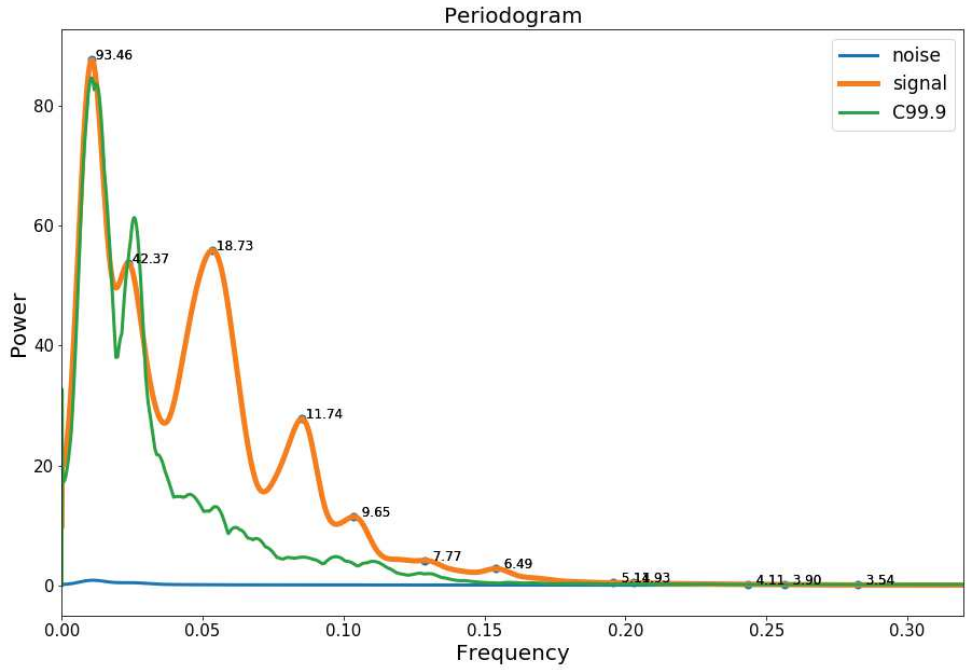

Figure 30: Mean periodogram of one of the selected radargrams (01286601). In orange is reported the spectrum for the signal measured in the region highlighted in blue in Figure 28. In blue is reported the spectrum of the noise, measured in the free space region highlighted in red in 28. In green it is possible to see an enhancement of the noise, in order to visualize his shape and behaviour. For each spectrum peak is indicated its relative period value in pixels.

As to understand the significance of the peaks in the periodograms, we made an estimation of the *red noise*. In fact, according to climatic models (Mann and Lees, 1996), our signal should be characterized by this type of noise, that has a decreasing power density with increasing frequency f ($\propto \frac{1}{f^2}$). This noise model is an *autoregressive model of the* 1° *order (AR1)* and it is characterized by two parameters. In order to obtain its spectrum we used *astrochron*, a R[1] package. In particular, we chose the *Multitaper method (MTM)* for spectral analysis, proposed by Thomson, 1982. MTM attempts to reduce the variance of spectral estimates by using a series of special data windows, rather than a unique data taper or a spectral window. All the tapers of the set are orthogonal to each other and belongs to a family of functions known as *discrete prolate spheroidal sequences (DPSS)* or *Slepian sequences* (Weedon, 2003). After each taper has been applied to the data a periodogram is generated. Thanks to the orthogonality, each periodogram is based on different weighting for different parts of the data and hence, the periodograms can be averaged (Percival, Walden, et al., 1993). This yields a better and more stable estimate, i.e. one with lower variance, than do single-taper methods. The resulting spectrum has well-suppressed side-lobes (i.e. small bias), good smoothing and yet high frequency resolution (Weedon, 2003).

We apply this calculations on 5 different equally spaced columns for each selected region. In Figure 31 are shown these columns for SHARAD radargram 01286601.

In this way it is possible to obtain another spectrum of the noise, with its relative *intervals of confidence*, and make a comparison with the one due to the signal. The result for SHARAD radargram 01286601 is shown in Figure 32.

Furthermore, we made a *F-test*. It is used to test for the presence of spectral peaks related to regular cyclic components with constant phase (Thomson, 1990). In other words, it allows to describe how much the shape of a peak deviates from a perfect

1 A free software environment for statistical computing and graphics.

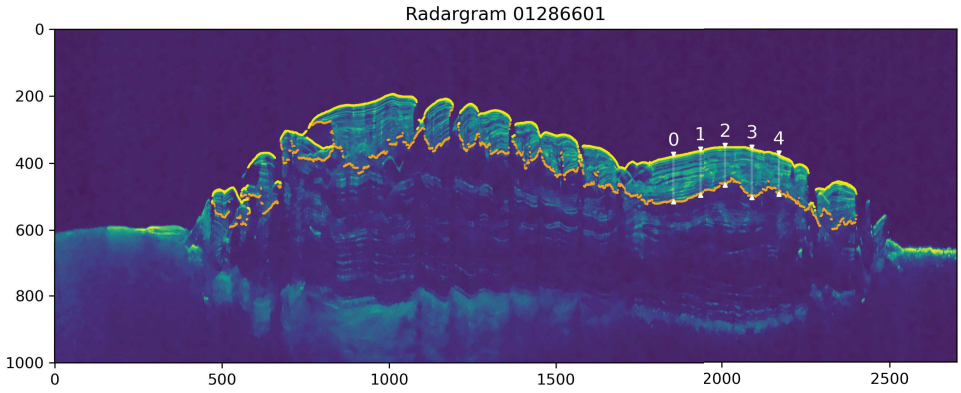

Figure 31: Selected time series for the red noise estimation of SHARAD radargram 01286601.

sinusoidal curve. The resulting confidence values are indicated in the upper part of Figure 32 with the blue peaks.

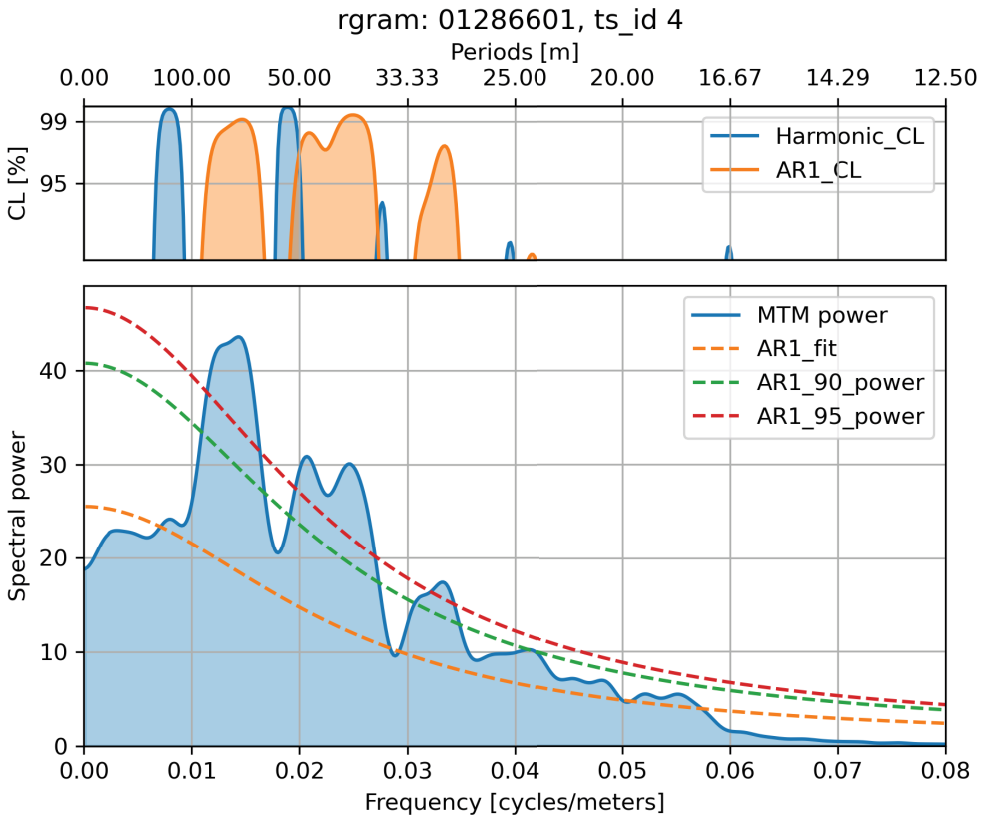

Figure 32: Spectrum of the signal of the 4 column of SHARAD radargram 01286601 (see Figure 31) with reported in orange the estimation of the red noise model (AR1-fit). In green and red are reported the two confidence curve at the 90% and 95% respectively. In the upper part is possible to see in orange the peaks that exceed the 90% confidence level, while in blue are indicated the products of the F-test.

6 RESULTS AND DISCUSSION

In the following we will show the results of the data analysis, whose phases have been described in detail in Chapter 5.

We applied the previously explained process on 10 different radargrams, the ones relative to the tracks selected homogeneously around the cap and showed in Figure 16. The track IDs of our sample are reported in the first column of table 1.

The isolation of the region of interest, through thresholding and labeling of connected component was succesfull and we can see the results summarized in Figure 33.

Then, we obtained one periodogram for each image. The spectral lines are not very narrow, but we expected this result because our time series are very short (on average they have a length of about 100 px), not allowing a high spectral resolution[1]. But having obtained many different periodograms, hence it was possible to average the values of the resulting important frequencies, measured on independent data, and thus reduce their oscillation in the spectrum.

In order to understand the significance of the spectrum peaks we analyzed two aspects:

1. the repetition of their periodicity inside the selected region.
2. the intervals of confidence obtained with the estimation of the red noise (explained at the end of Section 5.5.1).

In each periodogram it is possible to see one or two peaks with the greatest spectral energy, at the lower frequency values. We excluded them from our analysis because their corresponding periods in meters is approximately equal to the width of the selected region (obtained in Section 5.4), or repeated only two times inside of the selected regions. We decided to consider as significant only the wavelengths that are repeated at least 3 times inside the region of interest.

Furthermore these higher frequency peaks reflect the behaviour of the red noise and never appear to overcome even the 90% confidence level.

From the evaluation of peaks significance, it emerges that there are 3 main *spectral bands* in which the frequency peaks appear to be concentrated. The 1° defined by the interval 22.3 ± 4.73 px, the 2° by 13.24 ± 1.57 px, and the 3° by 9.41 ± 1.40 px. Every found periodicity for every band is reported in Table 1 in pixels unit. In Appendix A, it is possible to find all the 10 resulting periodograms with highlighted in orange, green and violet the boundaries of the three bands.

We made a comparison of our results with the periodicities found by Becerra, Sori, and Byrne, 2017. As anticipated in Section 4.2.2, Becerra, Sori, and Byrne, 2017 studied the layering periodicity, of the NPLD, thanks to 3 different types of stratigraphic observation, taken in several sites where the layers are exposed to the surface, and thus it is possible to investigate them through images and DTM models. Our 2° periodicity is in perfect agreement with the Long-Wavelenght one, reported in Table 2, obtained with the protrusion profiles and equal to 40.25 ± 2.56 m. Our 3° periodicity is close to the Short-Wavelenght one too, equal to 21.75 ± 1.63 m, but they are not completely in agreement.

In order to understand the connection with the variations of the orbital parameters, we calculated the *ratios* between the 3 layering periodicities, obtained from the

1 The explanation of this phenomenon lies in a consequence of the *uncertainty principle*. In fact, considering a *short* interval of time, that could be our time series, causes a *broadening in the conjugate frequency domain*, in this case widening the lines. In other words, the more a function, like a time series, is concentrated, the more spread out its Fourier transform will be.

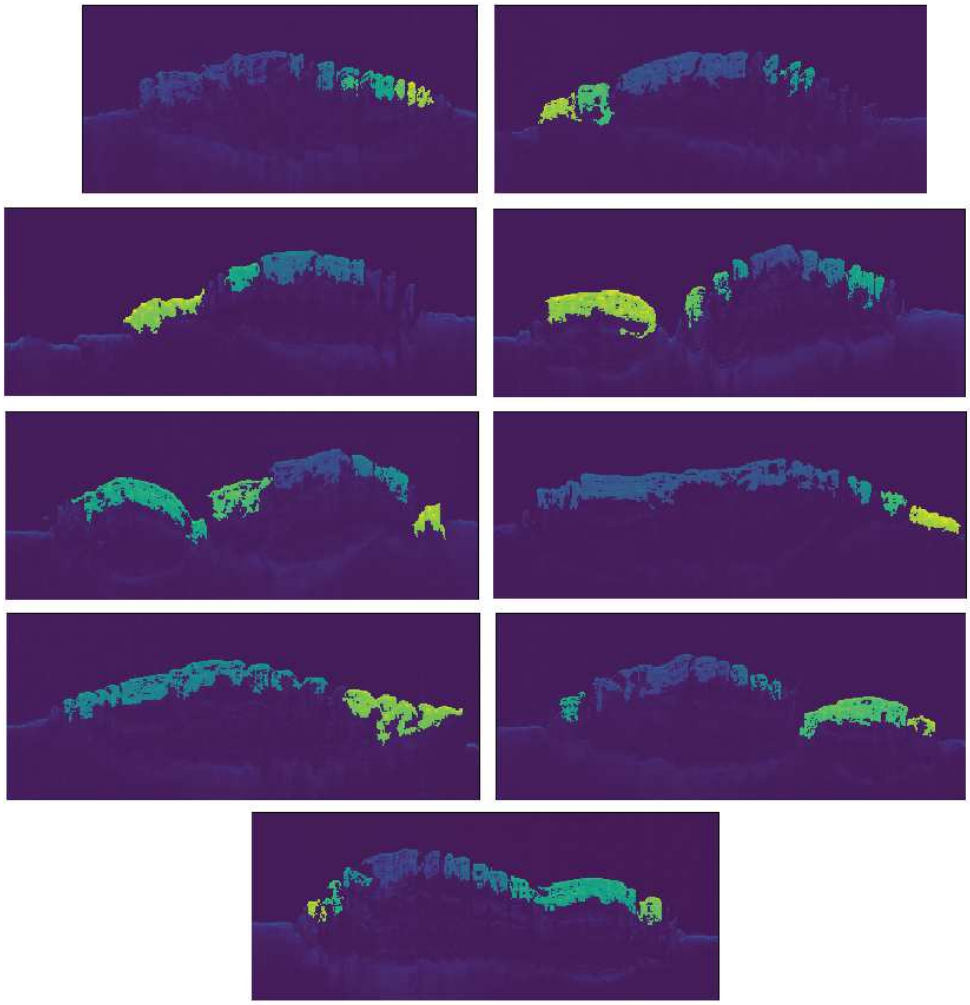

Figure 33: Summary vision of the final product of connected components operation on the 10 selected radargrams. The selected connected components are colored over the radar image.

Table 1: Periodicities found in the periodograms of each radar image, reported in pixel unit. In the last two rows there are the averaged values for each column in pixels and then converted in meters, with 1σ error bar.

Track ID	1° band periodicity	2° band periodicity	3° band periodicity
04523601	26.39	13.53	8.47
04236001	27.03	14.14	10.81
02181401	19.92	12.58	8.13
01321501	22.68	11.67	9.91
01399202	17.57	12.06	9.68
04441202	19.69	14.81	9.26
04260401	-	13.11	8.21
02022501	22.52	-	10.70
01286601	18.73	11.74	9.65
01373502	23.87	13.89	8.01
Averages [px]	22.04 ± 3.14	13.06 ± 1.06	9.28 ± 0.99
Averages [m]	69.82 ± 9.94	41.36 ± 3.34	29.40 ± 3.13

Table 2: Mean periodicities extracted from three different types of stratigraphic observations (indicated in the first column) by Becerra, Sori, and Byrne, 2017.

Stratigraphic profile type	Long-Wavelength [m]	Short-Wavelength [m]
Protrusion	40.25 ± 2.56	21.75 ± 1.63
Slope	17 ± 10.03	9 ± 1.70
Brightness	24.50 ± 2.62	11.00 ± 2.97

Table 3: Periodicity found through Laskar, Correia, et al., 2004 simulations.

Parameters	Periods [kyr]
Obliquity i	115.0 ± 16.4
Eccentricity e	97 ± 2
Argument of perihelion ω	50.0 ± 6.5

periodograms. Having found three main values, there is the possibility that each one of them is caused by the effect of one orbital parameter in particular. If this is true, these ratios should be similar to the ratios between the orbital parameters periods.

We considered the parameters periods of variations obtained by Laskar, Correia, et al., 2004, reported in Table 3, for martian obliquity i (which should not be confused with the inclination of the orbit, that refers to the angle between the reference plane and the plane of the orbit), eccentricity e and argument of perihelion ω. Then we calculated the ratios between each other and reported them in Table 4, together with the ratios obtained from the layering periodicity found in this work and by Becerra, Sori, and Byrne, 2017. There is only one ratio for Becerra, Sori, and Byrne, 2017 periodicities, because they indicate only two relevant ones.

Although we positioned Becerra, Sori, and Byrne, 2017 periodicities ratio in the column of the 2° to 3° ratio of the Table 4, because of the similarity to our relative periodicities, in their work they discuss only the possibility that these two wavelenght should be compared to the variation of the obliquity and the argument of perihelion, which would correspond to the 1° and 3° column of Table 1. This is because these two parameters in particular should have the major impact on the insolation curve (their ratio can be called indeed *insolaton ratio*). This last consideration should be theoretically correct, but dealing with a phenomenon that is not yet fully comprehended and very complex, we decided to not neglect the possible eccentricity effect, even because we found a third periodicity value that could be link to this orbital parameter. Even on the Earth, as previously explained in Section 3.1.1, the observed periodicity with the highest signal, from the mid Pleistocene transition onward (from $\sim 0.8 - 0.6\,Myr$ ago), matches the eccentricity period, even if this should be the weaker factor. In fact, Becerra, Sori, and Byrne, 2017 obtained a ratio which seems to agree more with the ratio due to eccentricity and precession periods. When they made the comparison with the ratio that takes into account obliquity and precession variations, they saw that it was greater then their periodicity ratio, deducing that NPLD formation should not be primarily driven by orbital control, or that the relationship between insolation (time) and accumulation (depth) in the NPLD should be nonlinear. But, taking into account the eccentricity, we obtained a ratio with the precession, that matches perfectly the one found by Becerra, Sori, and Byrne, 2017. Furthermore, the ratio that we found between the 1° and 3° periodicities agrees completely with the insolation ratio, suggesting that a possible link with the orbital forcing phenomenon can exist.

The other two found ratios (1° to 2° and 2° to 3°), in our case, do not correspond to the two remaining orbital period ratios. This opens the question on which ones of the obtained frequencies are correct and what are the real effects of the orbital forcing phenomenon. The successful matching between our 1° and 3° periodicities and the insolation ratio, gives hope that these two could be near to the correct

Table 4: Relevant layering periodicities (indicated by their order number 1°, 2°, 3°) ratios confronted with the ratios between the period of variation of Mars obliquity i, eccentricity e and argument of perihelion ω. Although the ratio which includes the two periodicities of Becerra, Sori, and Byrne, 2017 has been positioned in the 2° to 3° ratio column, originally they considered this ratio as the one between the 1° and 3° periodicities, because they didn't take into account the possible effect of eccentricity.

	1° to 2° ratio	2° to 3° ratio	1° to 3° ratio
Current work:	1.69 ± 0.28	1.40 ± 0.19	2.37 ± 0.42
Becerra, Sori, and Byrne, 2017:	-	1.93 ± 0.20	-
	i to e ratio	e to ω ratio	i to ω ratio
Laskar, Correia, et al., 2004:	1.18 ± 0.18	1.94 ± 0.26	2.30 ± 0.44

value. At the same time the two periodicities found by Becerra, Sori, and Byrne, 2017 give a good correlation too, if the effect of the eccentricity is included. The difficult point is that the 3° periodicity, that appears in both the two successful cases, is different for the two works and not much in agreement. Thus, which one of the two comes closest to real value? Or are they two different very close periodicities? Or maybe the connection between the 2° periodicity and the evolution of the eccentricity parameter is not that straightforward. In fact, we must also take into account that the variation of the eccentricity depends on the influence of several bodies of the Solar System, each of them acting with different entity and times scales. Thus, the different contributes can make the global eccentricity effect difficult to identify uniquely.

All of this questions need to be investigated with further analysis.

7 CONCLUSIONS

Our intention with this work was to study the influence of the *orbital forcing* phenomenon in the development of the stratification of the martian NPLD.

With this purpose, we decided to use *SHARAD radar data*, as to have a vast view of the interior of the cap and visualize the layering in all its extension. We selected 10 different radargrams, equally distributed around the cap, for the further analysis.

After finding out that exist a particular region, namely the one closest to the polar surface, were the layers are particularly bright and evident, which extends throughout the cap, and thus is visible in all the radargrams, we decided to isolate it, in order to extract the periodicities that characterize the succession of layers. These periodicities are important because they might provide a means of comparison with the variation of the orbital parameters.

After isolating the region of interest, through some algorithm of *image segmentation*, we extracted the relevant periodicities thanks to the *periodogram* method.

We noticed that the peaks in the spectra tend to gather in three bands. Finding a mean value for each one of these bands, allowed us to get three representative periodicities. After converting them from pixels to meters unit, we had three spatial periods that could be compared with the ones found by Becerra, Sori, and Byrne, 2017 and with the periods of variation of the orbital parameters.

In order to make this comparison, we calculated the ratios between the various found periodicities and we checked if they were in agreement with the ratios between the periods of variation of martian obliquity, eccentricity and argument of perihelion.

We found out that the ratio between our bigger periodicity and the smaller one perfectly matches the insolation ratio, i.e. the one between obliquity and argument of perihelion periods. This result could be very important in the understanding of the orbital forcing phenomenon, because it can be a proof of the influence of these two parameters, considered the ones that should have the major effect in this mechanism.

Furthermore, we took into account the influence of the eccentricity value, to see if its effect could coincide with our third found periodicity, the one with the middle value. Unfortunately, in this case the ratios are not in agreement with the remaining ones between the orbital parameters. Anyhow, we compared the ratios that involve the eccentricity with the ratio found by Becerra, Sori, and Byrne, 2017. We found a perfect agreement with the ratio between eccentricity and argument of perihelion periods. This thus gives hope for the confirmation that effectively the orbital forcing could have an important role in the NPLD region, and that the eccentricity's role is not to neglect. Even if, theoretically, this should be the weaker factor, both on the Earth and on Mars it seems to show its effects, sometimes even more than obliquity and precession. A probable explanation, as we mentioned in Section 3.1.1, is that, on both planets, there are several contributions to the climate that complicate the system. For example, there is the hypothesis that the 100 kyr Earth periodicity is probably the response of the *global carbon cycle*, on which the eccentricity seem to have an immediate effect and causes changes in atmospheric carbon dioxide concentration (Shackleton, 2000). Although Mars has a thinner and less dense atmosphere, with respect to the Earth, this could have a huge role too, considering also that it is primarily composed of carbon dioxide (95.32%).

Nevertheless there are still some unclear point: why our ratios that involve the 2° periodicity seem not to show to be in agreement with the eccentricity period provided by Laskar, Correia, et al., 2004, even with a different power with respect

to the insolation signal? Why the periodicity that should correspond to the influence of the precession does not correspond in the two study cases (this work and the one of Becerra, Sori, and Byrne, 2017)?

It is yet necessary to deepen this study and calculate with more precision all the periodicities, in order to answer to all the open questions.

7.1 FUTURE PROSPECTS

This work can be extended and improved in several ways.

With the purpose of improving the periodicities estimation, we could *improve our method*, to make it faster and more precise.

It could be useful to apply other types of image features recognition algorithm, so as to isolate the stratified region of interest in a faster and more automatic way, and so include many more radargrams to our analysis sample. This could be done by using feature descriptors or artificial intelligence algorithms, like the convolutional neural network, really much used in image and video recognition.

It could be also interesting to recognize in the image the bottom edge of the cap, in order to study the periodicity even in the deeper area. Since this part is older than the one isolated by us, it is interesting to understand if it is affected by the orbital parameters in the same way or if something has changed. For this purpose we could integrate our analysis with *MARSIS* radar data too. MARSIS has a lower vertical resolution with respect to SHARAD, but its signal can go deeper into the subsurface ($4-5\,\mathrm{km}$) and map some features that SHARAD can't reach.

Instead, to understand better the differences between our periodicity values and the ones found by Becerra, Sori, and Byrne, 2017, we could do a more in-depth study of the radar images that border their sites of study and see if we found the same periodicities or maybe if the layering that emerges to the surface has undergone some erosional processes or deposits of younger materials, that affect the periodicity evaluation.

Furthermore, this study can be extended to the *South polar cap* too, in order to understand the combined effect on the two caps of the orbital forcing phenomenon. This could be more difficult than in the northern case, because of the older age of the cap and the time limit of Laskar, Correia, et al., 2004 simulations. But Laskar, Correia, et al., 2004 provide also a statistical study of the evolution of the orbital parameters, that goes back to $\sim 250\,\mathrm{Myr}$, and we can use it to make a comparison with the resulting southern periodicities. The outcome of this further analysis can be confronted again with Becerra, Sori, Thomas, et al., 2019, that did the same analysis of Becerra, Sori, and Byrne, 2017 on the SPLD.

The questions that this work opens can give an additional reason for addressing the future Mars exploration to the polar cap regions. As explained by Thomas et al., 2019, currently the ESA plains for the future Mars missions focus on the *Human and Robotic Exploration (HER)* program, in order to have the possibility to participate in the *Mars Sample Return (MSR)* programme, led by NASA. Unfortunately, the polar cap regions are unlikely to be a goal of this program. But finding out more and more reasons to support the importance of other type of researches, could help the decision to plan a different type of future mission. In our case, it could be useful an orbiting mission, with a suitable near-polar orbit, equipped with a *radar of higher frequency*, with respect to SHARAD, as to obtain a more precise map of the layers, with a much higher vertical resolution (Thomas et al., 2019, Oberst, 2019). Even a *rover*, designed for the exploration of one of the two caps, could be helpful (Thomas et al., 2019). Even if there are many technical challenging aspects, it will be possible to get help from the experience, that will be gained with the ExoMars rover, Rosalind Franklin, whose launch has been postponed to 2022, and with Mars 2020 Perseverance rover (NASA).

In this way it could be possible to better decode the climatic information contained inside of the stratification, understand more and more the entity of the orbital forcing phenomenon on Mars and then apply the gained comprehension of the mechanism on other terrestrial planets.

A APPENDIX

In the following section, all the obtained periodograms will be reported, accompained by their relative radargram.

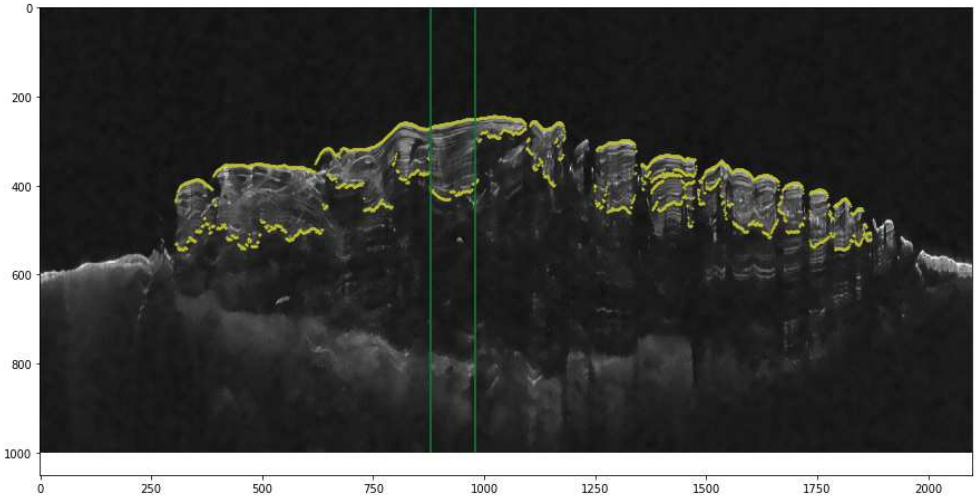

(a) *SHARAD radargram* 04523601. *The yellow points surround the region of interest, selected with the connected components method, and two green vertical lines delimit the restricted area chose for the spectral analysis.*

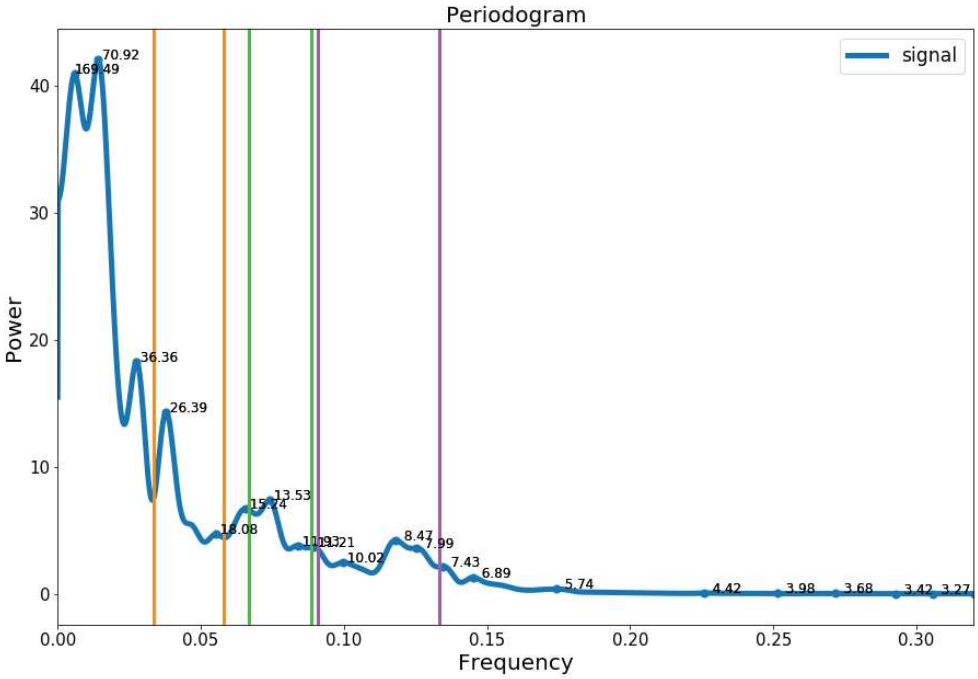

(b) *Periodogram relative to the area selected in the upper Figure. In orange, green and violet are reported the lines that delimits the three bands in which the peaks are principally concentrated.*

Figure 34: Image and periodogram of SHARAD radargram 04523601.

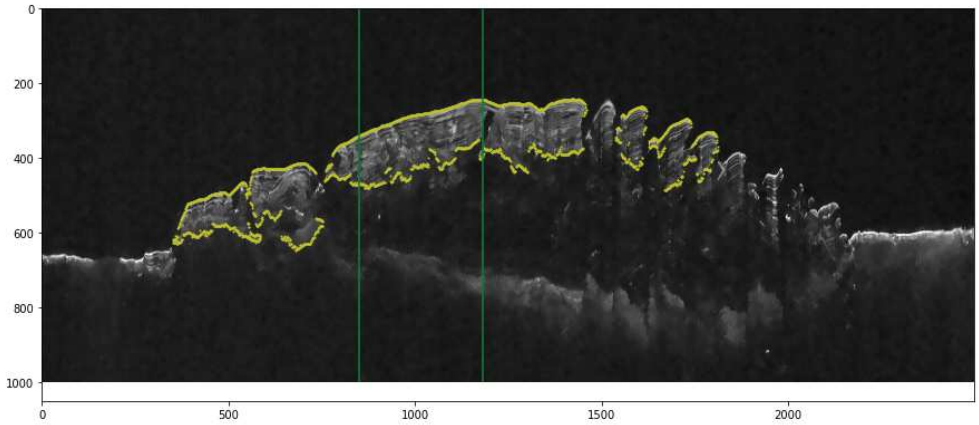

(a) *SHARAD radargram 04236001. The yellow points surround the region of interest, selected with the connected components method, and two green vertical lines delimit the restricted area chose for the spectral analysis.*

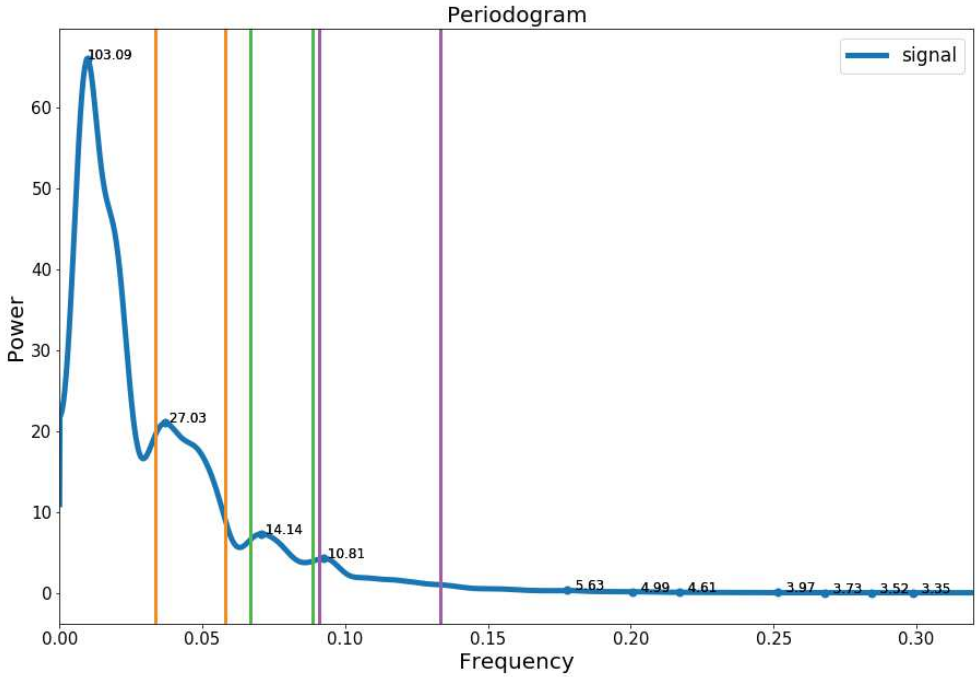

(b) *Periodogram relative to the area selected in the upper Figure. In orange, green and violet are reported the lines that delimits the three bands in which the peaks are principally concentrated.*

Figure 35: Image and periodogram of SHARAD radargram 04236001.

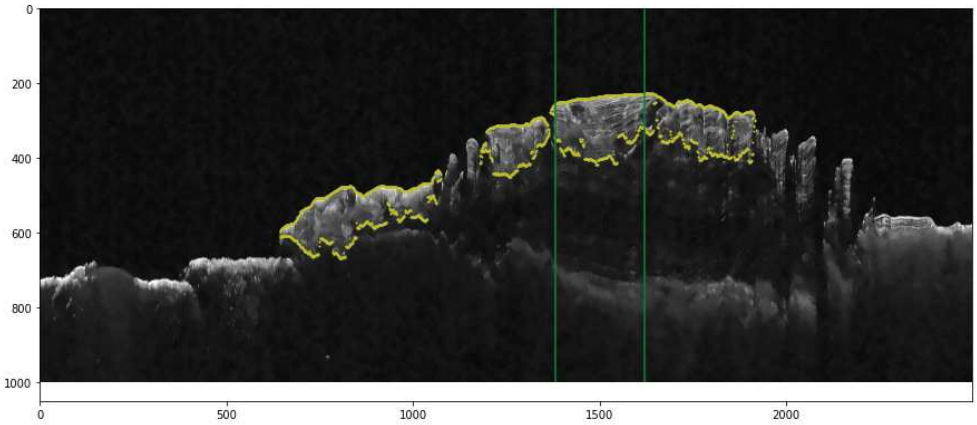

(a) *SHARAD radargram 02181401. The yellow points surround the region of interest, selected with the connected components method, and two green vertical lines delimit the restricted area chose for the spectral analysis.*

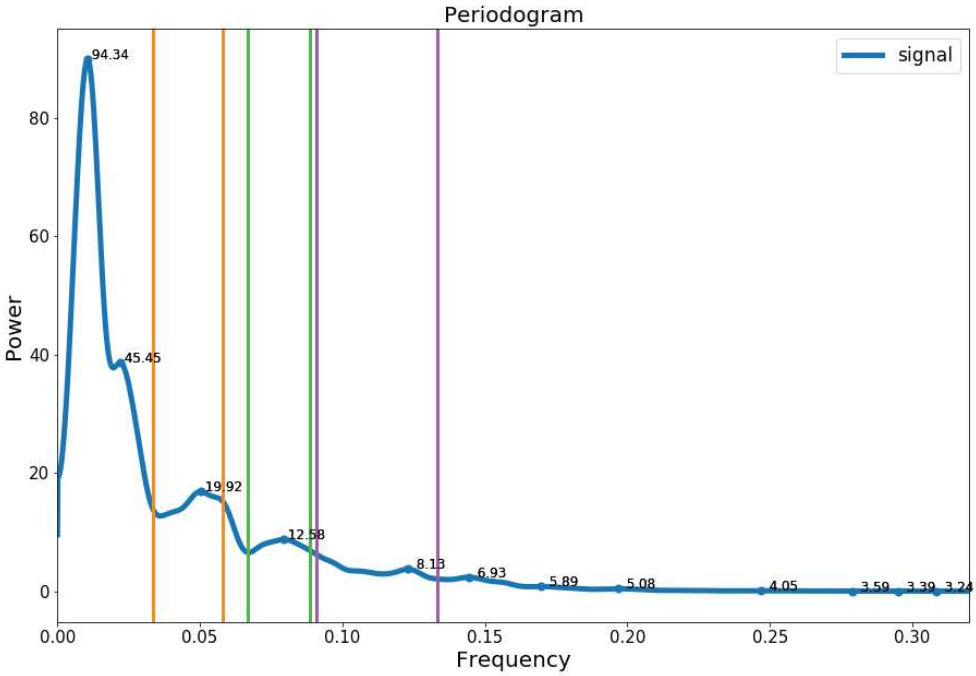

(b) *Periodogram relative to the area selected in the upper Figure. In orange, green and violet are reported the lines that delimits the three bands in which the peaks are principally concentrated.*

Figure 36: Image and periodogram of SHARAD radargram 02181401.

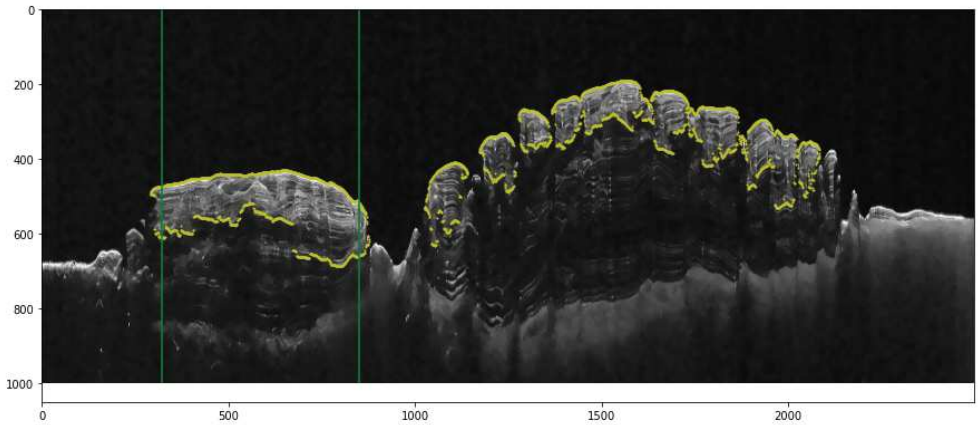

(a) *SHARAD radargram* 01321501. *The yellow points surround the region of interest, selected with the connected components method, and two green vertical lines delimit the restricted area chose for the spectral analysis.*

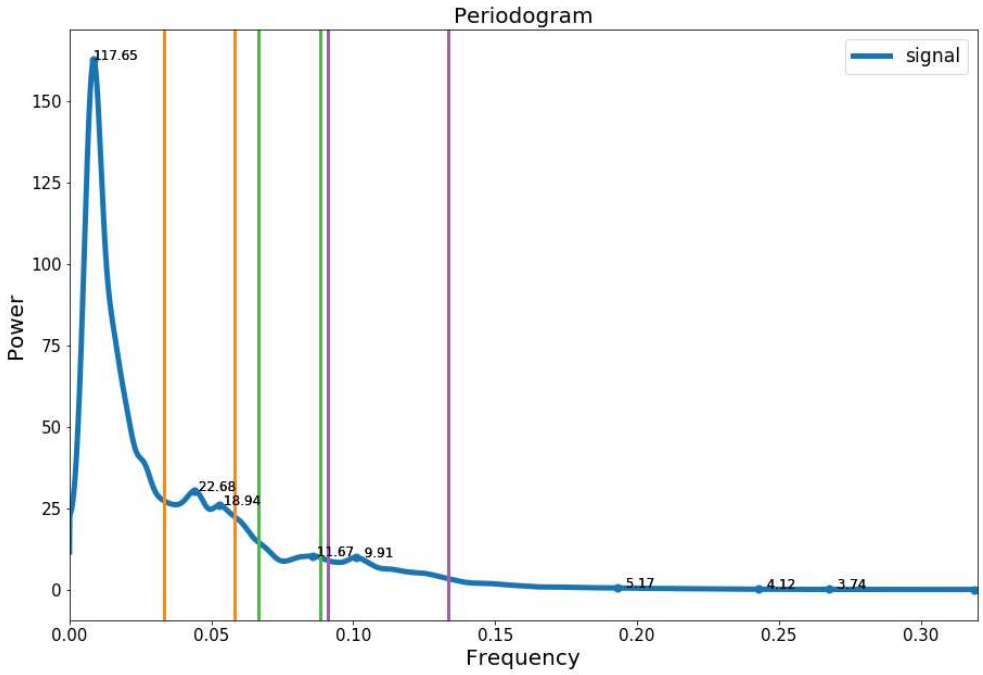

(b) *Periodogram relative to the area selected in the upper Figure. In orange, green and violet are reported the lines that delimits the three bands in which the peaks are principally concentrated.*

Figure 37: Image and periodogram of SHARAD radargram 01321501.

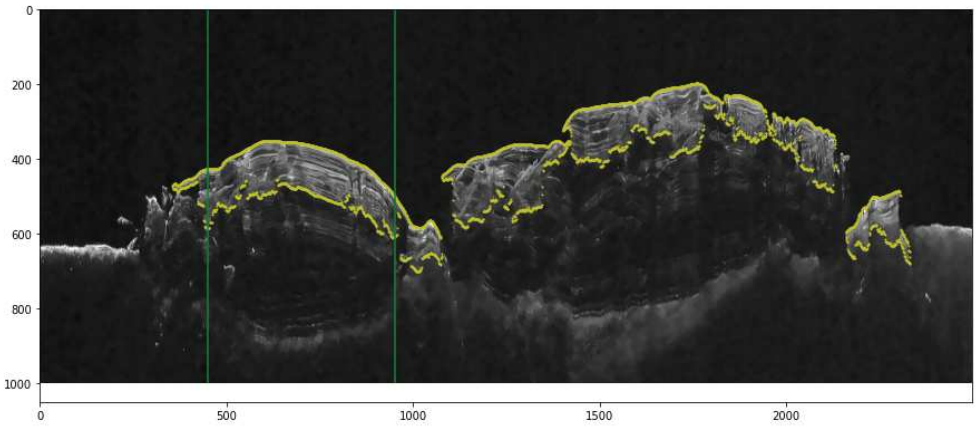

(a) *SHARAD radargram* 01399202. *The yellow points surround the region of interest, selected with the connected components method, and two green vertical lines delimit the restricted area chose for the spectral analysis.*

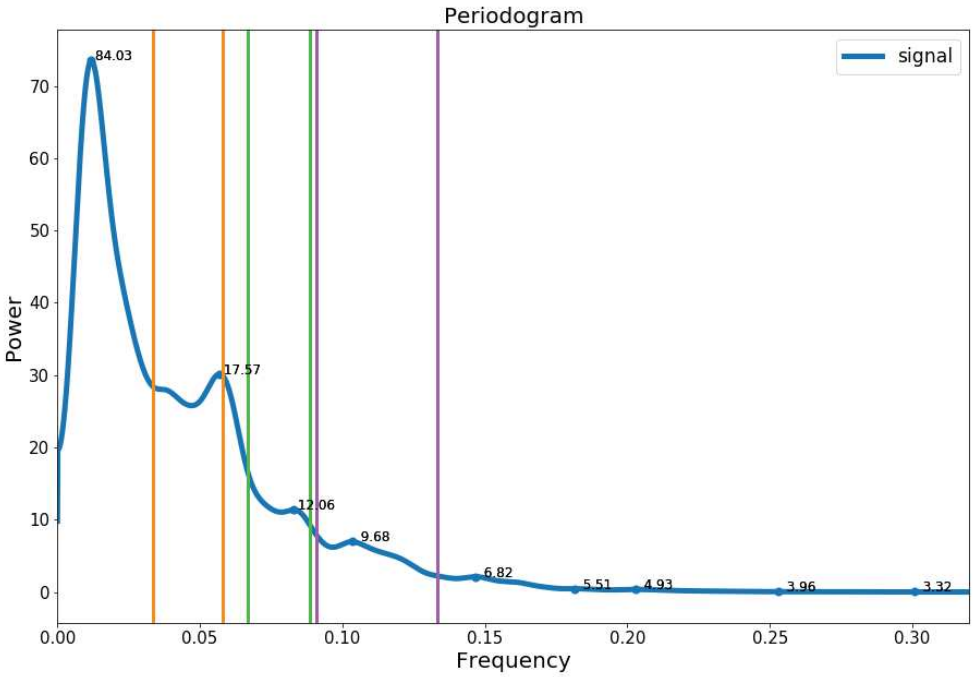

(b) *Periodogram relative to the area selected in the upper Figure. In orange, green and violet are reported the lines that delimits the three bands in which the peaks are principally concentrated.*

Figure 38: Image and periodogram of SHARAD radargram 01399202.

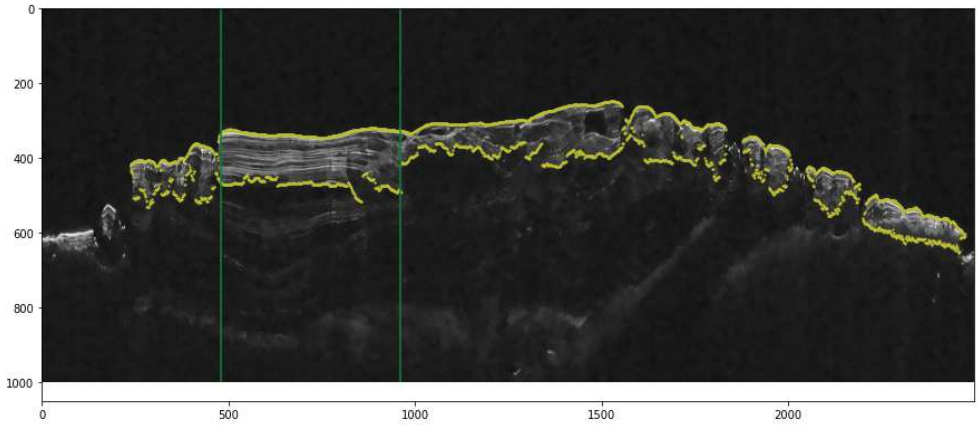

(a) *SHARAD radargram 04441202. The yellow points surround the region of interest, selected with the connected components method, and two green vertical lines delimit the restricted area chose for the spectral analysis.*

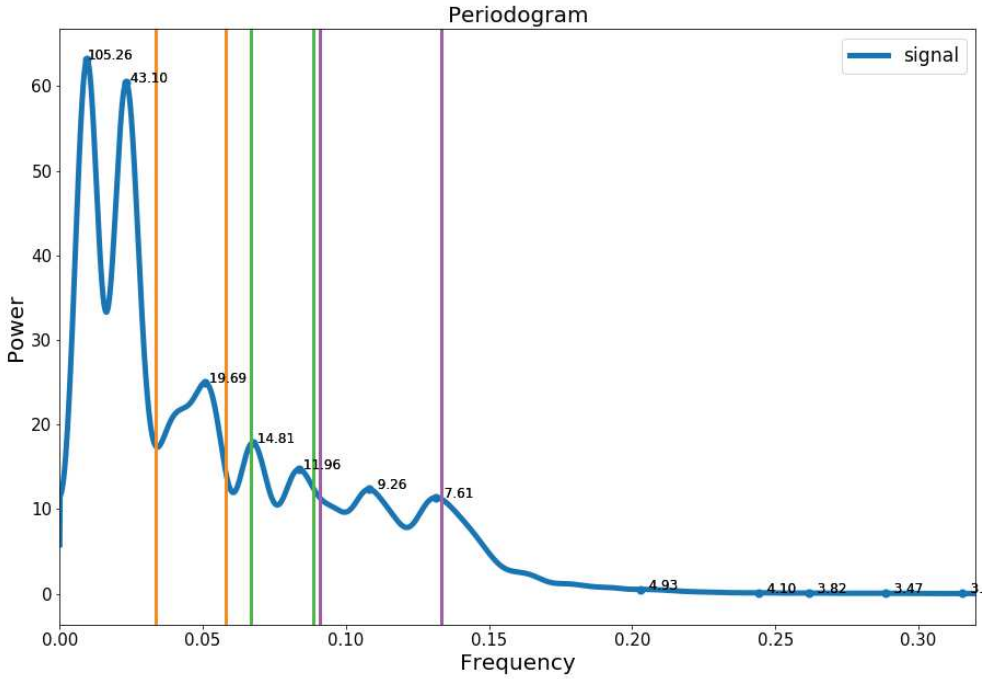

(b) *Periodogram relative to the area selected in the upper Figure. In orange, green and violet are reported the lines that delimits the three bands in which the peaks are principally concentrated.*

Figure 39: Image and periodogram of SHARAD radargram 04441202.

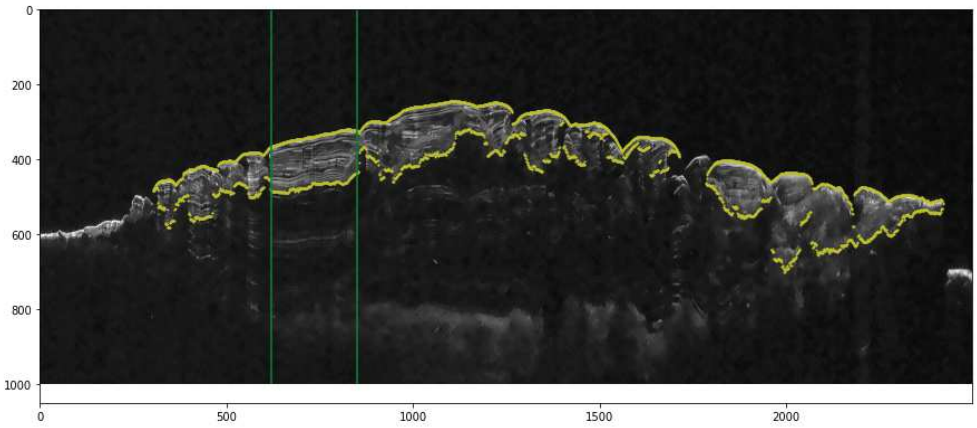

(a) *SHARAD radargram 04260401. The yellow points surround the region of interest, selected with the connected components method, and two green vertical lines delimit the restricted area chose for the spectral analysis.*

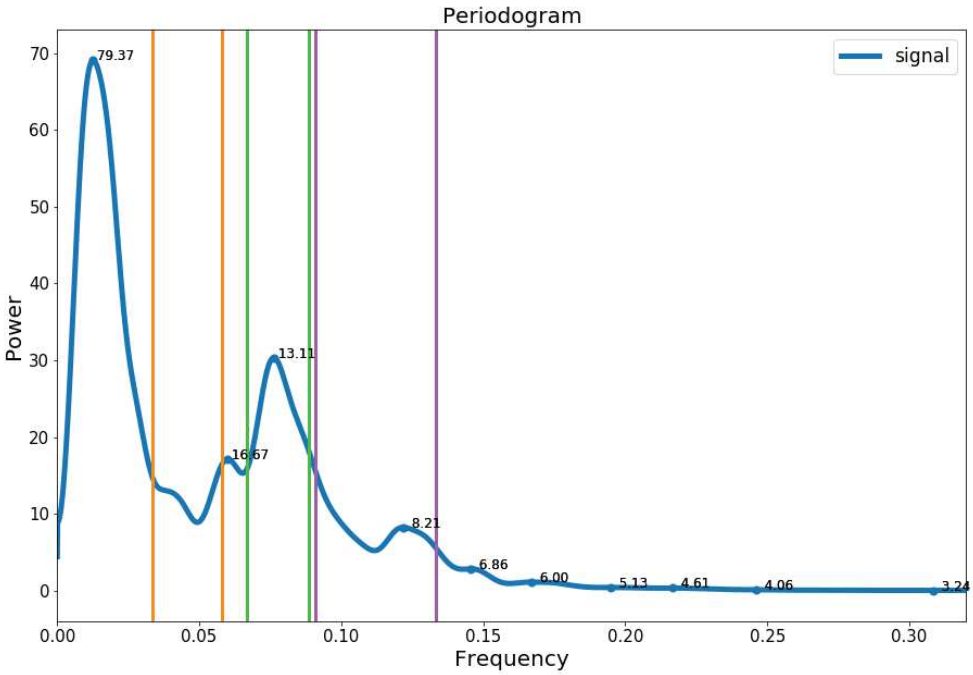

(b) *Periodogram relative to the area selected in the upper Figure. In orange, green and violet are reported the lines that delimits the three bands in which the peaks are principally concentrated.*

Figure 40: Image and periodogram of SHARAD radargram 04260401.

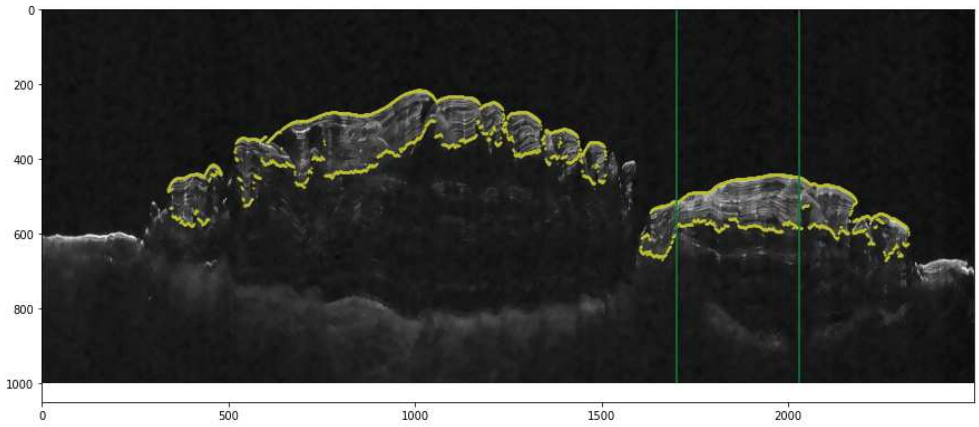

(a) *SHARAD radargram* 02022501. *The yellow points surround the region of interest, selected with the connected components method, and two green vertical lines delimit the restricted area chose for the spectral analysis.*

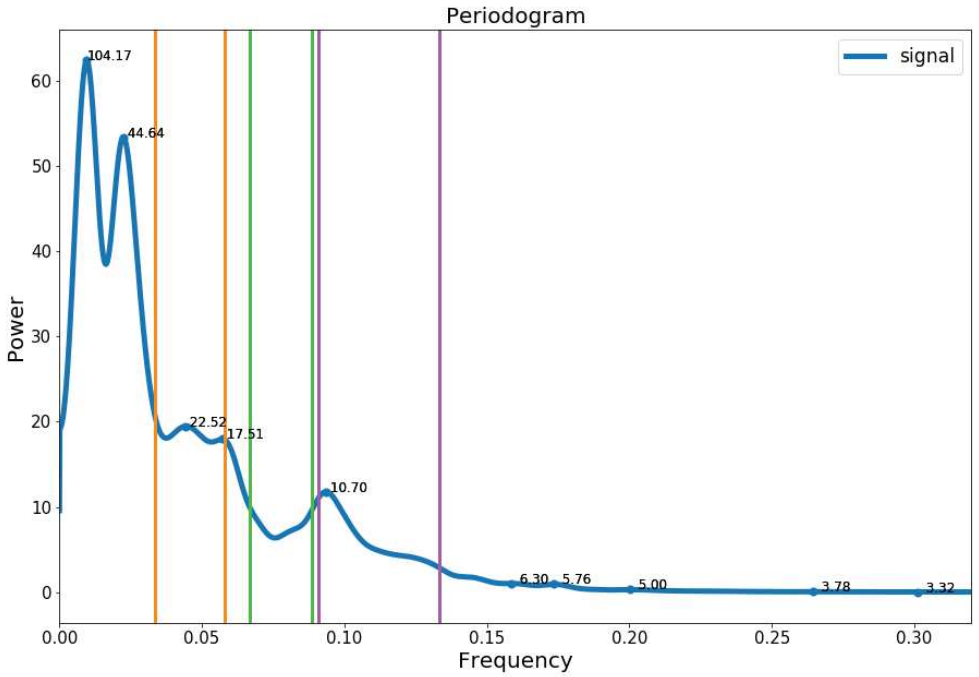

(b) *Periodogram relative to the area selected in the upper Figure. In orange, green and violet are reported the lines that delimits the three bands in which the peaks are principally concentrated.*

Figure 41: Image and periodogram of SHARAD radargram 02022501.

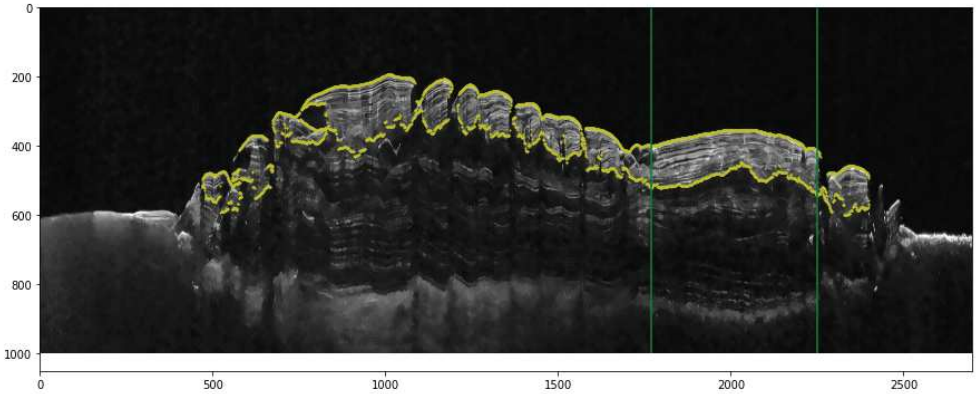

(a) *SHARAD radargram 01286601. The yellow points surround the region of interest, selected with the connected components method, and two green vertical lines delimit the restricted area chose for the spectral analysis.*

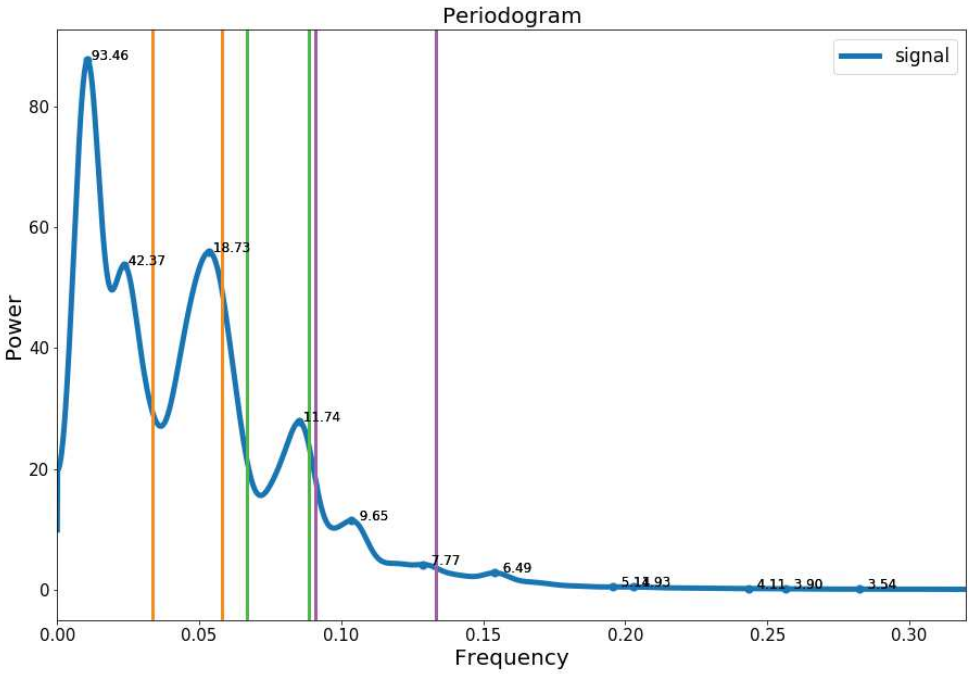

(b) *Periodogram relative to the area selected in the upper Figure. In orange, green and violet are reported the lines that delimits the three bands in which the peaks are principally concentrated.*

Figure 42: Image and periodogram of SHARAD radargram 01286601.

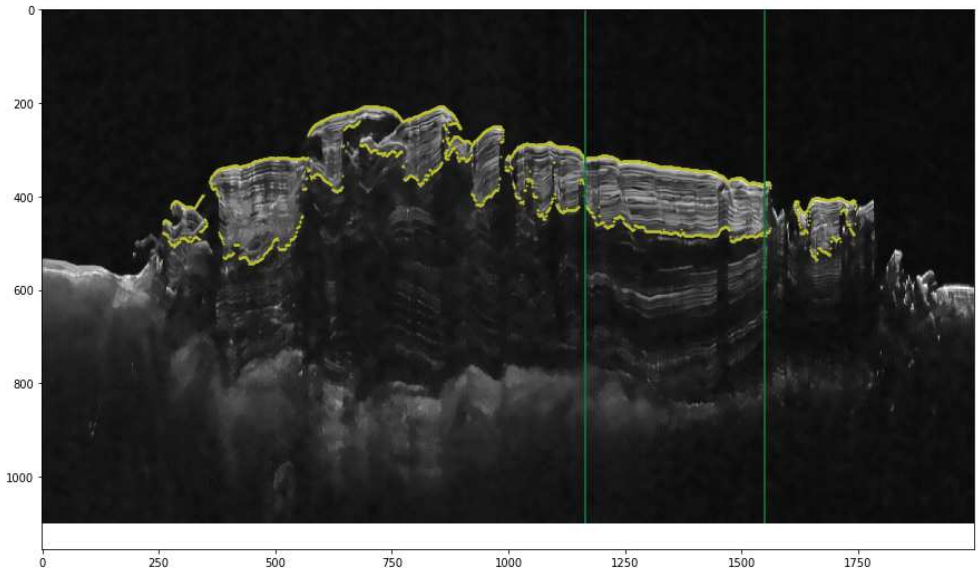

(a) *SHARAD radargram* 01373502. *The yellow points surround the region of interest, selected with the connected components method, and two green vertical lines delimit the restricted area chose for the spectral analysis.*

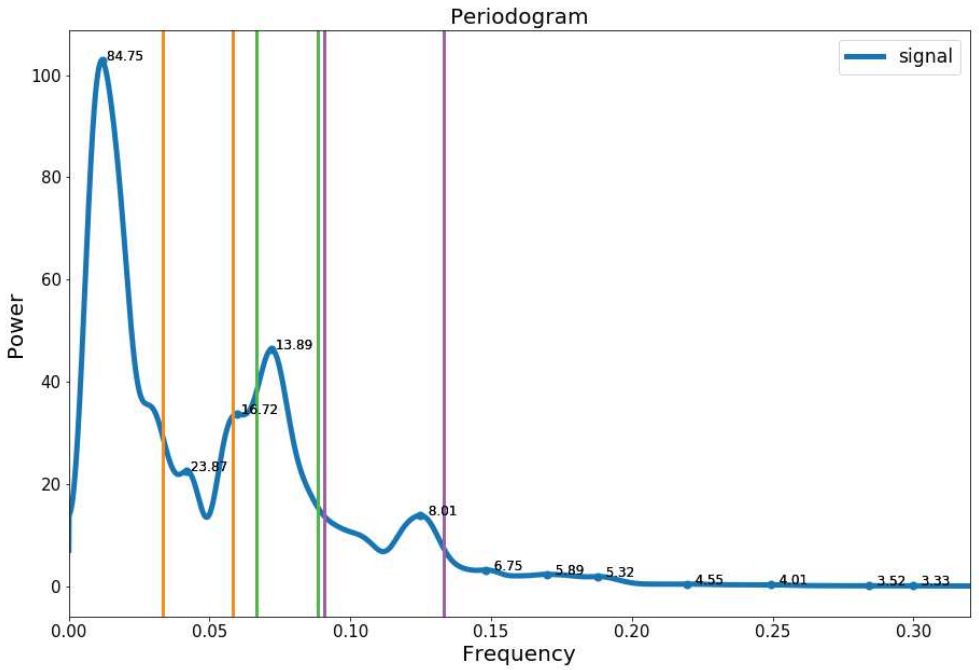

(b) *Periodogram relative to the area selected in the upper Figure. In orange, green and violet are reported the lines that delimits the three bands in which the peaks are principally concentrated.*

Figure 43: Image and periodogram of SHARAD radargram 01373502.

BIBLIOGRAPHY

Becerra, Patricio, Michael M Sori, and Shane Byrne

2017 "Signals of astronomical climate forcing in the exposure topography of the North Polar Layered Deposits of Mars," *Geophysical Research Letters*, 44, 1, pp. 62-70.

Becerra, Patricio, Michael M Sori, Nicolas Thomas, Antoine Pommerol, Emanuele Simioni, Sarah S Sutton, Stepan Tulyakov, and Gabriele Cremonese

2019 "Timescales of the climate record in the south polar ice cap of Mars," *Geophysical Research Letters*, 46, 13, pp. 7268-7277.

Berger, André

1988 "Milankovitch theory and climate," *Reviews of geophysics*, 26, 4, pp. 624-657.

Berger, André and Marie-France Loutre

1991 "Insolation values for the climate of the last 10 million years," *Quaternary Science Reviews*, 10, 4, pp. 297-317.

Bloomfield, Peter

2004 *Fourier analysis of time series: an introduction*, John Wiley & Sons.

Bogorodsky, Vitalii Vasilevich, Charles R Bentley, and PE Gudmandsen

2012 *Radioglaciology*, Springer Science & Business Media, vol. 1.

Broecker, Wallace S and Jan Van Donk

1970 "Insolation changes, ice volumes, and the O18 record in deep-sea cores," *Reviews of Geophysics*, 8, 1, pp. 169-198.

Buades, Antoni, Bartomeu Coll, and Jean-Michel Morel

2011 "Non-local means denoising," *Image Processing On Line*, 1, pp. 208-212.

Campbell, BA

2014 "US SHAllow RADar (SHARAD) Data Product Description for the Planetary Data System," *Smithsonian Institute: Washington, DC, USA*.

Campbell, BA and RJ Phillips

2014 "Mars reconnaissance orbiter shallow radar radargram data," in *NASA Planetary Data System, MRO-M-SHARAD-5-RADARGRAM-V1. 0*, NASA.

Chen, Wai Kai

2004 *The electrical engineering handbook*, Elsevier.

Clifford, SM

1980 "Chasma. boreale (85 n, 0 w): remnant of a martian jokulhlaup?" In *Bulletin of the American Astronomical Society*, vol. 12, p. 678.

Croll, James

1867 "LV. On the change in the obliquity of the ecliptic, its influence on the climate of the polar regions and on the level of the sea," *The London, Edinburgh, and Dublin Philosophical Magazine and Journal of Science*, 33, 225, pp. 426-445.

Dwivedy, Prashant, Anjali Potnis, and Madhuram Mishra

2017 "Performance Assessment of Several Filters for Removing Salt and Pepper Noise, Gaussian Noise, Rayleigh Noise and Uniform Noise," *Empirical Research Press Ltd.*, p. 176.

Edgett, Kenneth S, Rebecca ME Williams, Michael C Malin, Bruce A Cantor, and Peter C Thomas

2003 "Mars landscape evolution: Influence of stratigraphy on geomorphology in the north polar region," *Geomorphology*, 52, 3-4, pp. 289-297.

Faure, Gunter and Teresa Mensing

2007 *Introduction to planetary science*, Springer.

Ferro, Adamo

2011 *Advanced Methods for the Analysis of Radar Sounder and VHR SAR Signals*, PhD thesis, University of Trento.

Fishbaugh, Kathryn E, Shane Byrne, Kenneth E Herkenhoff, Randolph L Kirk, Corey Fortezzo, Patrick S Russell, and Alfred McEwen

2010 "Evaluating the meaning of "layer" in the Martian north polar layered deposits and the impact on the climate connection," *Icarus*, 205, 1, pp. 269-282.

Fishbaugh, Kathryn E and James W Head III

2002 "Chasma Boreale, Mars: Topographic characterization from Mars Orbiter Laser Altimeter data and implications for mechanisms of formation," *Journal of Geophysical Research: Planets*, 107, E3, pp. 2-1.

Fishbaugh, Kathryn E and Christine S Hvidberg

2006 "Martian north polar layered deposits stratigraphy: Implications for accumulation rates and flow," *Journal of Geophysical Research: Planets*, 111, E6.

Folkner, WM, CF Yoder, DN Yuan, EM Standish, and RA Preston

1997 "Interior structure and seasonal mass redistribution of Mars from radio tracking of Mars Pathfinder," *Science*, 278, 5344, pp. 1749-1752.

Foss, Frederick J, Nathaniel E Putzig, Bruce A Campbell, and Roger J Phillips

2017 "3D imaging of Mars' polar ice caps using orbital radar data," *The Leading Edge*, 36, 1, pp. 43-57.

Greve, Ralf

2008 "Scenarios for the formation of Chasma Boreale, Mars," *Icarus*, 196, 2, pp. 359-367.

Grima, Cyril, Wlodek Kofman, Jérémie Mouginot, Roger J Phillips, Alain Hérique, Daniela Biccari, Roberto Seu, and Marco Cutigni

2009 "North polar deposits of Mars: Extreme purity of the water ice," *Geophysical Research Letters*, 36, 3.

He, Lifeng, Yuyan Chao, Kenji Suzuki, and Kesheng Wu

2009 "Fast connected-component labeling," *Pattern recognition*, 42, 9, pp. 1977-1987.

Herkenhoff, Ken E and Jeffrey J Plaut

2000 "Surface ages and resurfacing rates of the polar layered deposits on Mars," *Icarus*, 144, 2, pp. 243-253.

Herkenhoff, Kenneth E, Shane Byrne, Patrick S Russell, Kathryn E Fishbaugh, and Alfred S McEwen

2007 "Meter-scale morphology of the north polar region of Mars," *Science*, 317, 5845, pp. 1711-1715.

Holt, John W, Kathryn E Fishbaugh, S Byrne, S Christian, K Tanaka, PS Russell, Kenneth E Herkenhoff, A Safaeinili, Nathaniel E Putzig, and RJ Phillips

2010 "The construction of chasma boreale on Mars," *Nature*, 465, 7297, pp. 446-449.

Hugenschmidt, J

2010 "Ground penetrating radar for the evaluation of reinforced concrete structures," in *Non-Destructive Evaluation of Reinforced Concrete Structures*, Elsevier, pp. 317-333.

Hvidberg, Christine S

2004 "6 Polar Caps," in *Water on Mars and Life*, Springer, pp. 129-153.

Hvidberg, Christine Schøtt, Kathryn E Fishbaugh, Mai Winstrup, Anders Svensson, Shane Byrne, and Kenneth E Herkenhoff

2012 "Reading the climate record of the Martian polar layered deposits," *Icarus*, 221, 1, pp. 405-419.

Jakosky, Bruce M, Bradley G Henderson, and Michael T Mellon

1995 "Chaotic obliquity and the nature of the Martian climate," *Journal of Geophysical Research: Planets*, 100, E1, pp. 1579-1584.

Kanasewich, Ernest R

1981 *Time sequence analysis in geophysics*, University of Alberta.

Kieffer, Hugh H, Philip R Christensen, and Timothy N Titus

2006 "CO 2 jets formed by sublimation beneath translucent slab ice in Mars' seasonal south polar ice cap," *Nature*, 442, 7104, pp. 793-796.

Koutnik, Michelle, Shane Byrne, and Bruce Murray

2002 "South polar layered deposits of Mars: The cratering record," *Journal of Geophysical Research: Planets*, 107, E11, pp. 10-1.

Laskar, Jacques

2004 "A comment on "Accurate spin axes and solar system dynamics: climatic variations for the Earth and Mars"," *Astronomy & Astrophysics*, 416, 2, pp. 799-800.

Laskar, Jacques, ACM Correia, Mickael Gastineau, Frédéric Joutel, Benjamin Levrard, and Philippe Robutel

2004 "Long term evolution and chaotic diffusion of the insolation quantities of Mars," *Icarus*, 170, 2, pp. 343-364.

Laskar, Jacques, Philippe Robutel, Frédéric Joutel, Mickael Gastineau, ACM Correia, and Benjamin Levrard

2004 "A long-term numerical solution for the insolation quantities of the Earth," *Astronomy & Astrophysics*, 428, 1, pp. 261-285.

Lauknes, Tom Rune

2011 "Rockslide mapping in Norway by means of interferometric SAR time series analysis."

Mann, Michael E and Jonathan M Lees

1996 "Robust estimation of background noise and signal detection in climatic time series," *Climatic change*, 33, 3, pp. 409-445.

MRO Press Kit, NASA

2006 "Mars Reconnaissance Orbiter Arrival."

Muller, Richard A and Gordon J MacDonald

1997a "Glacial cycles and astronomical forcing," *Science*, 277, 5323, pp. 215-218.

1997b "Simultaneous presence of orbital inclination and eccentricity in proxy climate records from Ocean Drilling Program Site 806," *Geology*, 25, 1, pp. 3-6.

Oberst, Jürgen

2019 *Planetary Polar Explorer: The Case for a Next-Generation Remote Sensing Mission to Low Mars Orbit*, https://www.cosmos.esa.int/documents/1866264/3219248/OberstJ_WhitePaperPlanetaryPolarExplorer__Oberst.pdf/ac9832ef-8f62-0eb3-f9cf-7cfedeb4b327?t=1565184650136.

Oliver, Chris and Shaun Quegan

2004 *Understanding synthetic aperture radar images*, SciTech Publishing.

Percival, Donald B, Andrew T Walden, et al.

1993 *Spectral analysis for physical applications*, cambridge university press.

Pettengill, GH, HW Briscoe, JV Evans, E Gehrels, GM Hyde, LG Kraft, R Price, and WB Smith

1962 "A radar investigation of Venus," *The Astronomical Journal*, 67, p. 181.

Phillips, Roger J, Maria T Zuber, Suzanne E Smrekar, Michael T Mellon, James W Head, Kenneth L Tanaka, Nathaniel E Putzig, Sarah M Milkovich, Bruce A Campbell, Jeffrey J Plaut, et al.

2008 "Mars north polar deposits: Stratigraphy, age, and geodynamical response," *Science*, 320, 5880, pp. 1182-1185.

Pierrehumbert, Raymond T

2010 *Principles of planetary climate*, Cambridge University Press.

Pilorget, C and F Forget

2016 "Formation of gullies on Mars by debris flows triggered by CO 2 sublimation," *Nature Geoscience*, 9, 1, pp. 65-69.

Putzig, Nathaniel E, Roger J Phillips, Bruce A Campbell, John W Holt, Jeffrey J Plaut, Lynn M Carter, Anthony F Egan, Fabrizio Bernardini, Ali Safaeinili, and Roberto Seu

2009 "Subsurface structure of Planum Boreum from Mars Reconnaissance Orbiter shallow radar soundings," *Icarus*, 204, 2, pp. 443-457.

Putzig, Nathaniel E, Isaac B Smith, Matthew R Perry, Frederick J Foss II, Bruce A Campbell, Roger J Phillips, and Roberto Seu

2018 "Three-dimensional radar imaging of structures and craters in the Martian polar caps," *Icarus*, 308, pp. 138-147.

Schuster, Arthur

1898 "On the investigation of hidden periodicities with application to a supposed 26 day period of meteorological phenomena," *Terrestrial Magnetism*, 3, 1, pp. 13-41.

Seu, Roberto, Roger J Phillips, Daniela Biccari, Roberto Orosei, Arturo Masdea, Giovanni Picardi, Ali Safaeinili, Bruce A Campbell, Jeffrey J Plaut, Lucia Marinangeli, et al.

2007 "SHARAD sounding radar on the Mars Reconnaissance Orbiter," *Journal of Geophysical Research: Planets*, 112, E5.

Shackleton, Nicholas J

2000 "The 100,000-year ice-age cycle identified and found to lag temperature, carbon dioxide, and orbital eccentricity," *Science*, 289, 5486, pp. 1897-1902.

Smith, Isaac B, Paul O Hayne, Shane Byrne, Patricio Becerra, Melinda Kahre, Wendy Calvin, Christine Hvidberg, Sarah Milkovich, Peter Buhler, Margaret Landis, et al.

2020 "The Holy Grail: A road map for unlocking the climate record stored within Mars' polar layered deposits," *Planetary and space science*, 184, p. 104841.

Soare, Richard J, Susan J Conway, and Stephen M Clifford

2018 *Dynamic Mars: Recent and Current Landscape Evolution of the Red Planet*, Elsevier.

Thomas, Nicolas, Patricio Becerra, and Isaac Smith

2019 *Mars and the Science Programme The case for Mars Polar Science*, https://www.cosmos.esa.int/documents/1866264/3219248/ThomasN_thomas_esa_white_paper_Mars_Polar_190803.pdf/8bb72c96-8855-fe48-f190-4ba67bf2c7c2?t=1565184671746.

Thomson, David J

1982 "Spectrum estimation and harmonic analysis," *Proceedings of the IEEE*, 70, 9, pp. 1055-1096.

1990 "Quadratic-inverse spectrum estimates: applications to palaeoclimatology," *Philosophical Transactions of the Royal Society of London. Series A: Physical and Engineering Sciences*, 332, 1627, pp. 539-597.

Touma, Jihad and Jack Wisdom

1993 "The chaotic obliquity of Mars," *Science*, 259, 5099, pp. 1294-1297.

Warner, Nicholas H and Jack D Farmer

2008 "Importance of aeolian processes in the origin of the north polar chasmata, Mars," *Icarus*, 196, 2, pp. 368-384.

Weedon, Graham P

2003 *Time-series analysis and cyclostratigraphy: examining stratigraphic records of environmental cycles*, Cambridge University Press.

Yoder, CF, AS Konopliv, DN Yuan, EM Standish, and WM Folkner

2003 "Fluid core size of Mars from detection of the solar tide," *Science*, 300, 5617, pp. 299-303.

Zurek, Richard W and Suzanne E Smrekar

2007 "An overview of the Mars Reconnaissance Orbiter (MRO) science mission," *Journal of Geophysical Research: Planets*, 112, E5.

ACKNOWLEDGEMENTS

Ringrazio Matteo Massironi per avermi fatto appassionare a quest'ambito con il suo corso, per avermi seguito con entusiasmo e per tutto l'aiuto che mi ha dato con le sue lettere di referenza. Ringrazio anche Patrizia per i consigli e l'interesse dimostrato verso questo lavoro.

Ringrazio Luca Penasa per avermi seguito, aiutato e spiegato tantissime cose, nonostante il disagio della quarantena.

Ringrazio Padova, che è diventata uno dei posti dove posso dire di sentirmi davvero a casa e che mi ha permesso di crescere in tantissimi aspetti diversi.

Ringrazio i miei genitori che mi sono stati vicini e mi hanno sostenuto in ogni modo possibile. Quindi grazie al mio papà che, nel suo modo da orsetto, mi dimostra sempre quanto crede in me, e grazie alla mia mamma che è anche il mio rametto canterino preferito.

Ringrazio Stivolo per essere il fratello migliore che potessi avere. Non vedo l'ora di tornare ad urlare "VALERIO" assieme.

Ringrazio mio nonno, per essere una delle persone più sensibili che io conosca. Ringrazio mia nonna, per la sua forza e per la sua intelligenza (anche se potrebbe essere anche un po' meno brava a Triominos e lasciarmi vincere qualche volta, eh).

Ringrazio la Vitto per essere entrata nella mia vita con i suoi abbracci avvolgenti, i suoi libri, i suoi consigli e il suo ruolo di nonna adottiva.

Ringrazio le mie amiche da una vita per aver condiviso con me ogni anno a partire dalla scuola materna. Laura, che mi ha accompagnato in ogni singola classe che ho frequentato e che mi ha dovuto sopportare anche quando sono spuntata nel suo dipartimento, che è felice quando un posto dal tetto sembra un edificio e che diventerà la più grande business woman *potenzadifuocoo*. Alice, che oltre a cercare sempre di inquietarmi con carezzine notturne, colpacci da stalker e occhi spalancati, è anche la mia adorabile nipotina, di cui sono tanto orgogliosa. Elisa, che dopo avermi conquistato alle elementari (lo dice anche il mio diario con la data in cui siamo diventate amiche), non ha mai smesso di darmi motivi per volerle bene e di considerarla una delle persone più uniche che esistano. Sara, con la quale ho condiviso interminabili sessioni a soprannominare ogni simpatico personaggio della Frinzi e della quale sono contenta di poter ascoltare i più disparati racconti, stilesaradallora.

Ringrazio Sherly perché nonostante la distanza ha trovato sempre il modo di starmi vicino, per questi sei anni di audio interminabili e perché che Watsy ci sarebbe senza Sherly?

Ringrazio infinitamente Martina e Fabio, per essere diventati fin da subito la mia famiglia padovana, per aver sempre cercato di difendermi da qualsiasi cosa, compresa me stessa, per aver sopportato i miei mille scleri con matite picchiettanti e per dimostrarmi sempre il loro affetto. Spero di riuscire a fare altrettanto. Ah e grazie per essere stati entrambi (o essere ancora), in qualche modo, sposati con me. E visto che ci siamo e la situazione non è per nulla strana, ringrazierei anche il resto della mia famiglia losca, in particolare lo zio malmostoso e la zia fata madrina.

Ringrazio anche chi ha reso questi anni di magistrale così meravigliosi. Grazie a Erica, con la quale ho iniziato e finito questo percorso, che è arrivata proprio nel momento in cui avevo bisogno di lei e non se ne è più andata. Grazie ad Amelia per le lunghe chiacchierate e per le ancora più lunghe risate per i motivi più disparati e per chiedersi sempre assieme a me domande importanti come: where did you come from, where did you go? Grazie a Robi per stare sempre in fissa con me e per condividere i migliori momenti disagio (anguria?). Grazie a Marti per la dolcezza, per le perfette imitazioni delle hostess, per gli aperitivi lacrimosi e per essere la best

narratrice di lupus. Grazie a LiaPiaMartaTartarughinaPoggibonsi per essere entrata nella mia vita con i suoi occhiali vistosi e la sua pazzia che mi portano sempre tanta allegra. Grazie a Andrea per essere il mio regista e book master preferito. Grazie a BollyBoy che condivide con me la passione per i shasshispaziali e compone mirabili canzoni alle 5 di mattina in mezzo alle colline toscane. Grazie a Tobbbi per le sue mille B rosse e per il black humor che mi fa tanto ridere ma non potrà mai superare il non trovare qualcosa che non posso dire in un cassonetto. Grazie a Luca Giusto per le mille cene buonissime dai tempi rilassati e per aver reso impossibile per la mia voce interiore pronunciare "undici" in modo normale.

Grazie a Piero, per essere comparso saltellando nella mia vita e averla resa veramente un po' troppo bella. Viva i velieri, i quartieri da esplorare, i mulini di campanelle, i terrazzi nascosti, i tramontini, le albealbelalbe, i PTBAH, i filmini e il tempo che non ci risponde mai, ma non importa. Aspetto quella collina.